

INVESTIGATION OF THE HIGH-PRESSURE BEHAVIOR OF AMPHIBOLES

A THESIS SUBMITTED TO THE GRADUATE DIVISION OF THE UNIVERSITY OF
HAWAI'I AT MĀNOA IN PARTIAL FULFILLMENT OF THE REQUIREMENTS FOR THE
DEGREE OF

MASTER OF SCIENCE
IN
EARTH AND PLANETARY SCIENCES

MAY 2019

By
TOMMY W. YONG

Thesis Committee:

Przemyslaw Dera, Chairperson

Bin Chen

Julia E. Hammer

Keywords: Amphibole, phase transition, high pressure, single-crystal X-ray diffraction,
crystallography, diamond anvil cell, synchrotron source

Acknowledgements

It has been my greatest privilege to have had the opportunity to conduct this research as a student of the University of Hawai'i at Mānoa. I owe my deepest gratitude to my advisor, Dr. Przemyslaw Dera, without whom it would not have been possible to complete this work. He opened my eyes to the field of high-pressure crystallography, for which I am eternally grateful for. It has been an absolute pleasure working with him over the last two years.

Additionally, I am extremely thankful for my committee members, Dr. Bin Chen and Dr. Julia E. Hammer, who provided valuable feedback throughout this project. I am tremendously grateful to have had the opportunity to take classes from the both of you and the knowledge that you both have imparted on me has been invaluable towards the completion of this thesis.

I also owe a great debt of gratitude to Dr. Robert Downs and Dr. Hexiong Yang for inspiring me to continue my education in the geosciences and for their mentorship during my undergraduate studies. Many thanks go to my research group, Dr. Hannah Shelton, Dr. Dongzhou Zhang, Dr. Gregory Finkelstein, Dr. Yi Hu and May Chornkrathok for serving as role models, colleagues and friends throughout my time in Hawai'i and Chicago.

I would like to thank the support from the Fred M. Bullard Endowed Graduate Fellowship, National Science Foundation Grant EAR-1722969 and EAR-1541516, the Department of Earth Sciences at the University of Hawai'i at Mānoa and Hawai'i Institute of Geophysics and Planetology.

Lastly, this thesis would not have been possible without the support of my parents and wife-to-be, Lauren Ward. You are my greatest supporters, my pillar of strength and my inspiration, without you none of this would have been possible.

Abstract

Amphibole group minerals are important constituents in many metamorphic and igneous rocks. They have an unusually high chemical variety, which allows them to be used as petrogenetic indicators. Owing to their structural and chemical complexity, developments on quantitative descriptions of amphiboles have been hindered. High-pressure structural studies using a synchrotron X-ray source were conducted on two different amphibole mineral species, namely, grunerite ($\text{Fe}_7\text{Si}_8\text{O}_{22}(\text{OH})_2$) and gedrite ($\text{Mg}_2(\text{Mg}_3\text{Al}_2)(\text{Si}_6\text{Al}_2)\text{O}_{22}(\text{OH})_2$). In both minerals, new pressure-induced displacive phase transitions are observed around 20 GPa that closely mirror the phase-transition sequences known in pyroxenes. The phase transitions are characterized by a greater degree of kinking in the double silicate chains of tetrahedra. The experimental findings of this study demonstrate the parallel pressure-induced phase transformation behavior between amphiboles and pyroxenes, suggesting that structures with comparable topology behave similarly in response to high-pressure. In the lithospheric mantle, amphiboles are the most abundant hydrous species, consequently they play an important role in numerous petrological and geophysical processes, such as partial melting and devolatilization. The geophysical implications of the experimental findings of this study are discussed in terms of subducting slabs along disequilibrium pathways that deviate from an average mantle geotherm. The metastable persistence of amphibole group minerals into higher-pressure regimes may have possible implications towards slab buoyancy or as a potential trigger for seismic events.

Table of Contents

Acknowledgements.....	i
Abstract.....	ii
List of Tables	iv
List of Figures.....	v
Chapter 1. Introduction.....	1
1.1 Thesis Overview	1
1.2 Introduction to Amphiboles	2
1.3 Overview of Common Amphibole Crystal Structures.....	3
Chapter 2. Single crystal X-ray Diffraction of Grunerite up to 25.6 GPa: A New High-Pressure Clinoamphibole Polymorph.....	9
2.1 Introduction.....	10
2.2 Experimental Procedures	11
2.3 Results and Discussion	16
2.4 Implications.....	22
2.5 Tables and Figures	25
Chapter 3. A New High-Pressure Phase Transition in Natural Gedrite.....	33
3.1 Introduction.....	34
3.2 Experimental Procedures	35
3.3 Results.....	40
3.4 Discussion.....	44
3.5 Tables and Figures	50
Chapter 4. Conclusions and Future Work.....	60
References.....	63

List of Tables

2.1 Microprobe analyses of grunerite	25
2.2 Single-crystal structure refinement details.....	26
2.3 Unit cell parameters of grunerite	26
2.4 Atomic positional coordinates of grunerite.....	27
2.5 Bond lengths of grunerite.....	28
2.6 Equation of state data for grunerite.....	28
3.1 Microprobe analyses of gedrite.....	50
3.2 Microprobe analyses of standards.....	51
3.3 Hydrogen bond distances.....	51
3.4 Single-crystal structure refinement details.....	51
3.5 Atomic positional coordinates of gedrite	52
3.6 Anisotropic displacement parameters of gedrite.....	55
3.7 Unit cell parameters of gedrite.....	55
3.8 Polyhedra volumes and distortion parameters of gedrite.....	56

List of Figures

1.1 $C2/m$ amphibole structure	5
1.2 $Pnma$ amphibole structure	7
1.3 $P2_1/m$ amphibole structure	8
2.1 Grunerite (α , β , γ) crystal structure	29
2.2 Normalized unit cell parameters of grunerite	30
2.3 Chain displacement factor in grunerite	30
2.4 Unit cell volume of grunerite	30
2.5 Kinking angle of grunerite	30
2.6 M4-O5 distance in grunerite	31
2.7 M4-O6 distance in grunerite	31
2.8 Atomic coordination of M4 site in grunerite	31
2.9 M4 polyhedral configuration in grunerite	32
2.10 Density of grunerite, ferrosilite and PREM	32
3.1 Gedrite (α , β) crystal structure	57
3.2 I-beam topological representation of various amphibole phases	58
3.3 Atomic coordination of the M4 site in gedrite	59
3.4 M4 polyhedral configuration in gedrite	59

Chapter 1. Introduction

1.1 Thesis Overview

Amphibole group minerals undergo a series of pressure induced phase transitions that closely resemble those of the pyroxenes. This thesis investigated the high-pressure behavior of two amphibole group minerals namely grunerite, $\text{Fe}_7\text{Si}_8\text{O}_{22}(\text{OH})_2$, and gedrite, $\text{Mg}_2(\text{Mg}_3\text{Al}_2)(\text{Si}_6\text{Al}_2)\text{O}_{22}(\text{OH})_2$. Quantitative information obtained through X-ray diffraction techniques was used to properly document the structural changes and compressibility behavior associated with each mineral species. Petrological and geophysical implications for the experimental findings of this thesis are discussed.

Chapter 1 provides the geophysical context and background information on the amphibole group of minerals and the crystal structures of amphiboles that are studied in this thesis.

Chapter 2 investigates the structural and compressional behavior of grunerite up to 25.6 GPa by single-crystal X-ray diffraction. A new phase of grunerite is observed and this study is the first structural report to show the existence of three polymorphs within an amphibole group mineral. The crystal structure of the new phase of grunerite was solved and showed to be isometric with the ambient pressure crystal structure. The results from chapter 2 illustrate the analogous phase transition behavior between monoclinic amphiboles and clinopyroxenes.

Chapter 3 covers the single-crystal X-ray diffraction of gedrite up to 27.7 GPa. A new monoclinic polymorph of gedrite is observed and this study is the first to show a pressure-induced phase transition of an orthoamphibole. The crystal structure of the new gedrite polymorph was solved. This chapter demonstrates that both orthorhombic amphiboles and orthopyroxenes display parallel phase transformation mechanisms.

1.2 Introduction to Amphiboles

Amphiboles are one of the most important rock-forming mineral groups in the Earth's crust and upper mantle. The general formula for an amphibole group mineral is $AB_2C_5T_8O_{22}W_2$, where A includes Na^+ , K^+ , Ca^{2+} , and Li ; B includes Na^+ , Li^+ , Ca^{2+} , Mn^{2+} , Fe^{2+} , and Mg^{2+} ; C includes Mg^{2+} , Fe^{2+} , Mn^{2+} , Al^{3+} , Fe^{3+} , Mn^{3+} , Ti^{4+} , and Li^+ ; T includes Si^{4+} , Al^{3+} , and Ti^{4+} ; and W includes $(OH)^-$, F^- , Cl^- , O^{2-} . Amphiboles belong to a group of minerals known as inosilicates, which are characterized by chains of silica tetrahedra. They are widespread in altered oceanic crust, subducting slabs, and in metamorphic and igneous rocks. Out of the major rock forming minerals the amphibole group displays the widest range of parageneses and chemical composition (Hawthorne 1981). As a result of their common occurrence and unique chemistry, amphibole minerals are potentially among the most powerful petrogenic indicators (Hirschmann et al. 1994). Additionally, amphiboles are a dominant repository of water and volatiles within the Earth's crust and upper mantle. Understanding the stability, crystal chemical relationships, physical properties and energetics of this mineral group are essential in modeling large scale geologic processes such as magma generation and slab subduction owing to the hydrous component of amphiboles. Because of the complex nature of amphiboles, our current understanding of the amphibole group has not progressed as rapidly as compared to the less complex silicate minerals.

Structural studies of the amphibole group minerals have been well documented at ambient conditions. However, despite their ubiquity, relatively few structural studies have been conducted under high-pressure conditions. Previous high-pressure structural studies have been conducted at pressures below 10 GPa (Comodi et al. 1991; Zhang et al. 1992; Yang et al. 1998; Welch et al. 2007; Comodi et al. 2010; Zanazzi et al. 2010; Welch et al. 2011; Nestola et al. 2012). Studies at

pressures greater than 10 GPa have involved spectroscopic characterization (Iezzi et al. 2006; Iezzi et al. 2009; Iezzi et al. 2011; Thompson et al. 2016), but not structural refinement.

The relationship between the chemistry, physical properties and parageneses of the pyroxenes (single-chain inosilicates) and amphiboles (double-chain inosilicates) were established in the 1930s (Warren 1930; Warren and Modell 1930a; Carpenter 1982). The first amphibole structure solution was approached by analogy with known structures of pyroxenes (Warren 1930). Clino- and orthopyroxenes both undergo pressure-induced phase transitions (Brown et al. 1972; Hugh-Jones et al. 1994; Arlt et al. 1998; Arlt et al. 2000; Yang and Prewitt 2000; Tribaudino et al. 2001; Nestola et al. 2008; Zhang et al. 2012; Dera et al. 2013a; Finkelstein et al. 2015). Because of the structural association with amphiboles, higher pressure phases of both monoclinic and orthorhombic amphiboles have been proposed. With the advancements of *in situ* high-pressure X-ray diffraction techniques, structural investigations on the high-pressure behavior of amphiboles are now more easily attainable.

1.3 Overview of Common Amphibole Crystal Structures

The amphibole crystal structure is characterized by double chains of tetrahedra which extend along the [001] direction. A band of octahedrally coordinated cations, which also extend in the *c*-direction, designated by sites M(1), M(2), M(3) and M(4), link adjacent chains of tetrahedra along the *a*-axis. The tetrahedrally coordinated sites are denoted by 'T'. The double chains of tetrahedra form a six-membered ring, situated in the center of the ring is the A site. Currently, there are six known ambient structural variations of amphibole group minerals (Hawthorne and Oberti 2007). The minerals studied in this thesis have space group symmetries $C2/m$, $P2_1/m$ and $Pnma$.

The $C2/m$ amphibole structure

The crystal structure of the ambient $C2/m$ structure viewed down the a -axis is shown in figure 1.1. Amphiboles with $C2/m$ symmetry include the calcic amphiboles, sodic-calcic amphiboles, alkali amphiboles and monoclinic C -centered (Mg-Fe-Mn-Li) amphiboles (Hawthorne and Oberti 2007). Some examples include grunerite, actinolite and glaucophane. There is one type of double chain in the $C2/m$ structure, that contains two independent T sites, T(1) and T(2). T(1) is coordinated to O(1), O(5), O(6) and O(7), while T(2) is coordinated to O(2), O(4), O(5) and O(6). T(1) and T(2) tetrahedra link at O(5) and O(6) to form a chain of tetrahedra extending along [001], while adjacent T(1) tetrahedra link across O(7) to form double chains. The apex of the tetrahedra alternate along [010] across each double chain.

M(1) is an octahedrally coordinated site with point symmetry 2, that is coordinated to two O(1) and O(2) oxygen atoms, and to two O(3) W anions. M(2) is a octahedrally coordinated site with point symmetry 2, that is coordinated to two O(1), O(2) and O(4) oxygen atoms. The M(3) site is 6-coordinated with point symmetry $2/m$ and is coordinated to four O(1) oxygen atoms and two O(3) W anions. The M(4) site has point symmetry 2 and is situated at the fringe of the strip of octahedra (M(1), M(2) and M(3)). The M(4) site is surrounded by eight oxygen atoms, O(2) x 2, O(4) x 2, O(5) x 2 and O(6) x 2, not all of which necessarily bond to the M(4) cation. The M(4) site may be extremely distorted and vary from 6 to 8 coordination depending on the type of cation situated at the site.

The strip of octahedra (M site cations) link to the double chain of tetrahedra at O(4) oxygen atoms, which is coordinated to T(2) and M(2), along [010]. There is an additional linkage across the double chain to the strip of octahedra along [100] by the O(1) and O(2) oxygen atoms, which are situated on the apex of the T(1) and T(2) tetrahedra, respectively.

The A-site (see figure 1.2.) is situated in the center of the large cavity between adjacent double chains of tetrahedra along [100], within the six-membered ring of tetrahedra. The cavity is surrounded by twelve oxygen atoms, O(5) x 4, O(6) x 4, and O(7) x 4, not all of which necessarily bond to the A cations. The center of the cavity has point symmetry $2/m$, but generally A cations occupy off-centered positions of point symmetry 2 or m .

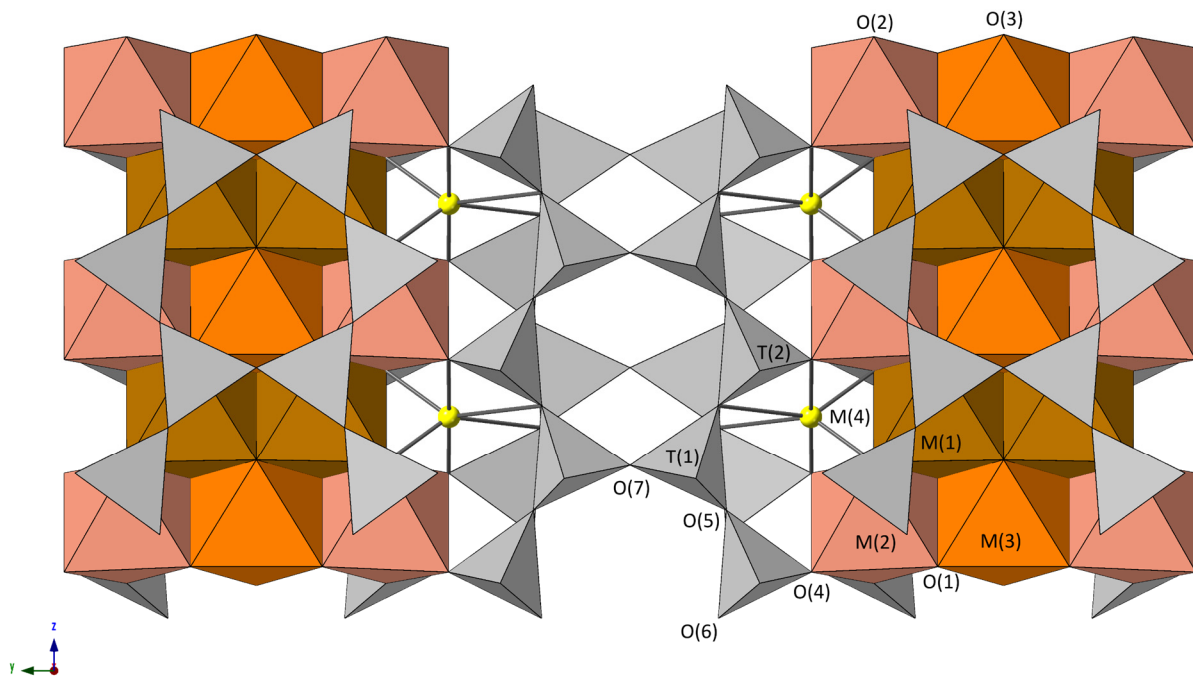


Figure 1.1. The $C2/m$ amphibole structure projected down [100].

The *Pnma* amphibole structure

Amphiboles with *Pnma* symmetry include the orthorhombic Mg-Fe-Mn amphiboles such as gedrite, anthophyllite and holmquistite (Hawthorne and Oberti 2007). The crystal structure of the ambient *Pnma* structure viewed down [100] is shown in figure 1.2. The *Pnma* structure contains two distinct double silicate chains, the A-chain and B-chain. There are four unique T-sites, labeled T(1A), T(2A), T(1B) and T(2B). Coordination and linkages of the T-sites is analogous to the *C2/m* structure, cations labelled 'A' are coordinated to anions labelled 'A' and cations labelled 'B' are bonded to anions labelled 'B'; for example, T(1A) is coordinated to O(1A), O(5A), O(6A) and O(7A), while T(1B) is coordinated to O(1B), O(5B), O(6B) and O(7B). The A-chain and B-chain alternate along [100], forming a stacking sequence: B-chain, strip of octahedra, A-chain.

The M(1) site has point symmetry 1, and is coordinated to O(1A), O(1B), O(2A) and O(2B) oxygen atoms, and O(3A) and O(3B) W anions. The M(2) site has point symmetry 1, and is coordinated to O(1A), O(1B), O(2A), O(2B), O(4A) and O(4B) oxygen atoms. The M(3) site has point symmetry *m*. and is bonded to O(1A) x 2 and O(1B) x 2 oxygen atoms, and O(3A) and O(3B) W anions. The M(4) site has point symmetry 1 and is surrounded by eight oxygen atoms, both A and B-type of O(2), O(4), O(5) and O(6).

The A site is situated in the center of the cavity within the six-membered ring of tetrahedra, in between back-to-back double chains. Unlike the *C2/m* structure, A site cations occupy the special position at the center of the cavity with point symmetry *m*.

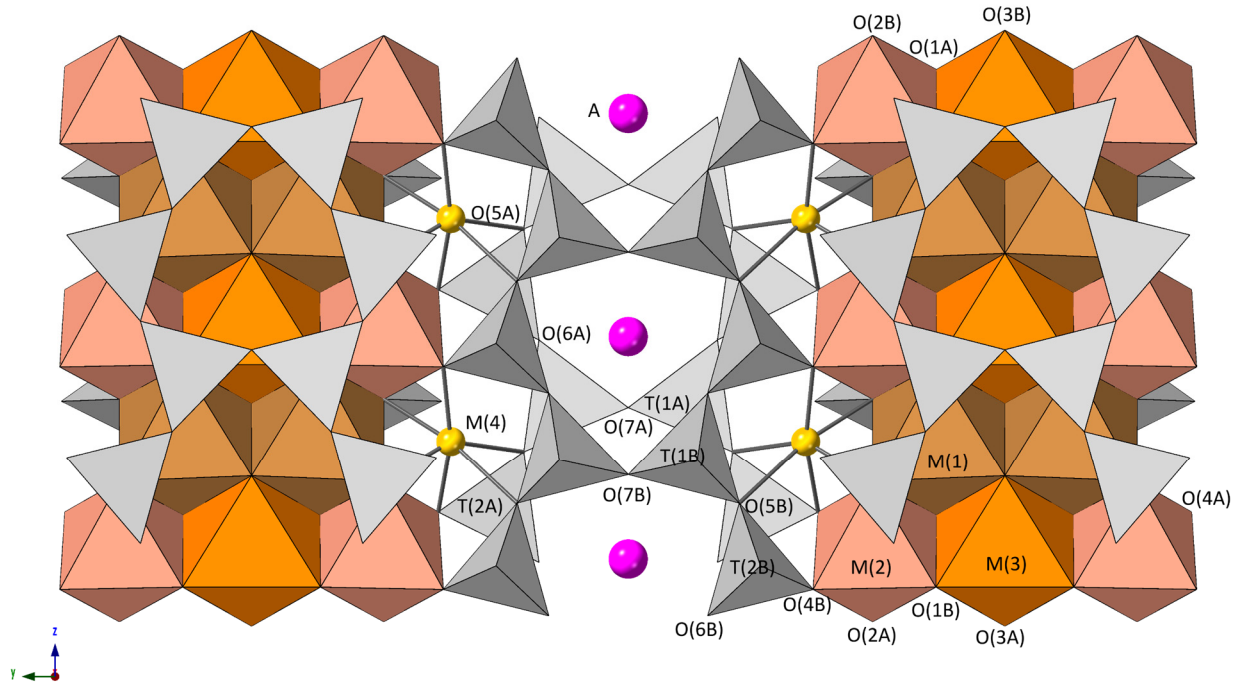


Figure 1.2. The *Pnma* amphibole structure projected down [100].

The $P2_1/m$ amphibole structure

The crystal structure of the ambient $P2_1/m$ structure viewed down [100] is shown in figure 1.3. Amphiboles that have $P2_1/m$ symmetry include cummingtonite and synthetic amphiboles with $\text{Na}(\text{Na},\text{Li},\text{Mg})_2\text{Mg}_5\text{Si}_8\text{O}_{22}(\text{OH})_2$ composition (Hawthorne and Oberti 2007). The $P2_1/m$ structure is comparable to the *Pnma* structure, containing two non-equivalent silicate chains, also called the A-chain and B-chain. Site symmetries and linkages are the same as the *Pnma* structure except the M(3) site has point symmetry m , due to the reduction in symmetry from orthorhombic to monoclinic.

The A-site is not generally included for the $P2_1/m$ structure as all known natural amphiboles with this space group have an unoccupied A site.

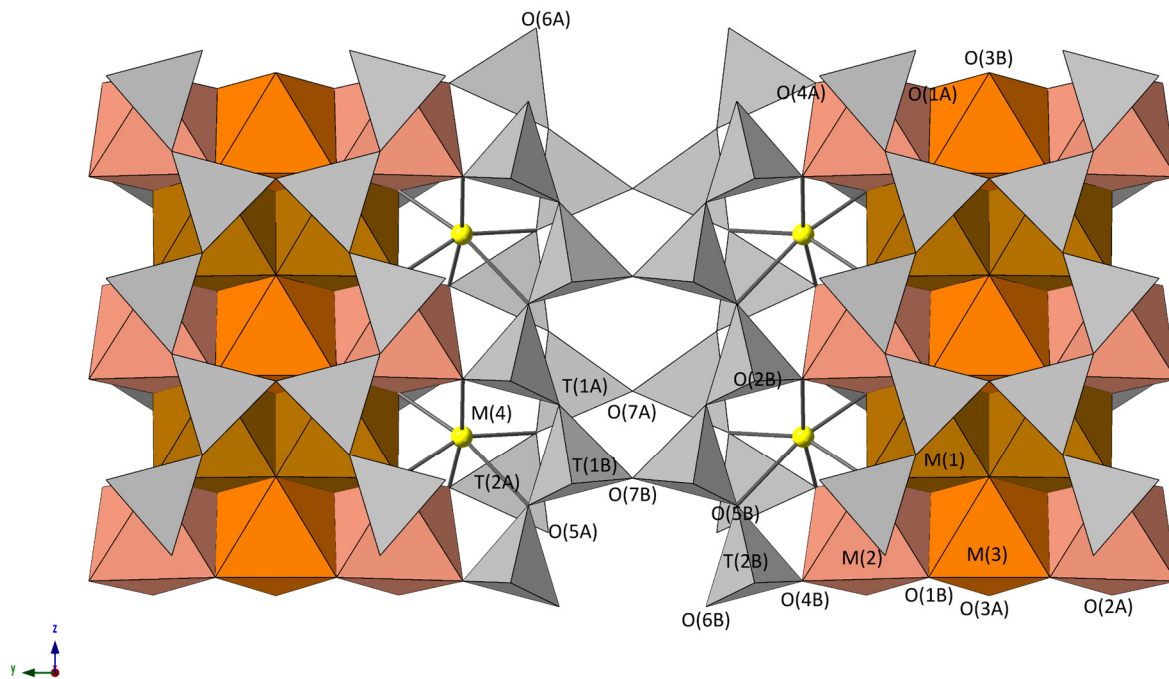


Figure 1.3. The $P2_1/m$ amphibole structure projected down $[100]$.

The high-pressure investigation of these structures will reveal novel phase transitions that are characterized by changes in M4 site coordination, greater kinking in the double silica chains, change in rotation type of the chains and site splitting.

Chapter 2. Single crystal X-ray Diffraction of Grunerite up to 25.6

GPa: A New High-Pressure Clinoamphibole Polymorph

Abstract

High-pressure single-crystal X-ray diffraction experiments were conducted on natural grunerite crystals using a synchrotron X-ray source with composition $(\text{Fe}_{5.237}\text{Mg}_{1.646}\text{Ca}_{0.061}\text{Mn}_{0.051}\text{Na}_{0.015}\text{Ti}_{0.002}\text{Cr}_{0.001}\text{K}_{0.001})(\text{Si}_{7.932}\text{Al}_{0.083})\text{O}_{22}(\text{OH})_2$. Grunerite has $C2/m$ symmetry at ambient conditions. The samples were compressed at 298 K in a diamond-anvil cell to a maximum pressure of 25.6(5) GPa. We observe a previously described phase transition from $C2/m$ (α) to $P2_1/m$ (β) to take place at 7.4(1) GPa, as well as a further transition from $P2_1/m$ (β) to $C2/m$ (γ) at 19.2(3) GPa. The second-order Birch-Murnaghan equation of state fit to our compressional data, yielded the values $V_0 = 914.7(7) \text{ \AA}^3$ and $K_0 = 78(1) \text{ GPa}$ for α -grunerite, $V_0 = 926(5) \text{ \AA}^3$ and $K_0 = 66(4) \text{ GPa}$ for β -grunerite and $V_0 = 925(27) \text{ \AA}^3$ and $K_0 = 66(13) \text{ GPa}$ for γ -grunerite. The $\beta - \gamma$ phase transition produces a greater degree of kinking in the double silicate chains of tetrahedra accompanied by a discontinuous change in the a and c unit cell parameters and the monoclinic β angle. At 22.8(4) GPa the O5-O6-O5 kinking angle of the new high-pressure $C2/m$ phase is $137.5(4)^\circ$, which is the lowest reported for any monoclinic amphibole. This study is the first structural report to show the existence of three polymorphs within an amphibole group mineral. The high-pressure γ -phase illustrates the parallel structural relations and phase transformation behavior of both monoclinic single and double chain silicates.

This chapter has been published as:

Yong, T., Dera, P. & Zhang, D. (2018). Single crystal X-ray Diffraction of Grunerite up to 25.6 GPa: A New High-Pressure Clinoamphibole Polymorph. Phys Chem Minerals. <https://doi.org/10.1007/s00269-018-0999-1>

2.1 Introduction

The cummingtonite-grunerite solid solution is of structural significance and interest as this binary join has three different ambient structural phases, orthorhombic *Pnma* anthophyllite (Mg end-member), monoclinic *P2₁/m* Mg-rich cummingtonites and monoclinic *C2/m* grunerites. Earlier experiments on the cummingtonite-grunerite solid solution series have shown that grunerite (Fe end-member, $\text{Fe}_7\text{Si}_8\text{O}_{22}(\text{OH})_2$) undergoes a phase transition from *C2/m* (α) to *P2₁/m* (β) with increasing pressure (Yang et al. 1998; Boffa Ballaran et al. 2000), while *P2₁/m* Mg-rich cummingtonites transforms to *C2/m* at high temperature (Prewitt et al. 1970).

The main difference between the *C2/m* and *P2₁/m* structure is that the *C2/m* phase contains one crystallographically distinct O-rotated silicate chain, while the *P2₁/m* structure contains two double silicate chains: the S-rotated A chain and O-rotated B chain (see Papike and Ross (1970) for a description of S- and O- rotated chains). Furthermore, the M4 site cation increases its coordination from 6 to 7 after the *C2/m*-*P2₁/m* phase transition.

Spectroscopic experiments on a synthetic amphibole with composition, $\text{Na}(\text{NaMg})\text{Mg}_5\text{Si}_8\text{O}_{22}(\text{OH})_2$ and *P2₁/m* ambient symmetry, have indicated a possible existence of a new high-pressure phase characterized by a C-centered lattice, with the phase transition likely to occur between 20 – 22 GPa (Iezzi et al. 2006). This new high-pressure phase change may be analogous to the structural changes seen in clinopyroxenes with increasing pressure, however, the previous study did not include structure determination. In order to shed new light on the nature of the higher-pressure amphibole phases we reinvestigated the compressional behavior of natural grunerite using synchrotron-based single crystal X-ray diffraction experiments. In this study, we report the existence of a previously unknown phase transition in natural grunerite between 16.3(3) and 19.2(3) GPa from *P2₁/m* (β) to *C2/m* (γ).

2.2 Experimental Procedure

Chemical analysis

In this study, we used a natural grunerite sample from Moose Mountain Mine, Ontario, Canada. The composition was determined by wavelength-dispersive spectrometry (WDS) using a JEOL Hyperprobe JXA-8500F. Peaking on standards were done at 15 keV, 20 nA and a beam diameter of 10 μm . Background corrections were based on measurements either side of the peak during off-peak measurements using a linear correction. Calibration was done at 15 keV, 10 nA and using a beam 10 μm in diameter. Three spot analyses on two different standards, treated as unknowns, were captured before and after analyses on the samples to look for instrumental errors. Analyses were done with the same analytical conditions as the calibration. The $K\alpha$ lines were used for all elements analyzed. Count times were 30 seconds on peak and 15 seconds on each off-peak position, except for measuring Ca, Cl and K where on peak positions were measured for 20 seconds and off-peak positions for 10 seconds. Full ZAF corrections to the background-corrected intensities for each spot were made using the Probe for EPMA software (Donovan et al. 2012). The composition of the natural grunerite sample was calculated to be $(\text{Fe}_{5.237}\text{Mg}_{1.646}\text{Ca}_{0.061}\text{Mn}_{0.051}\text{Na}_{0.015}\text{Ti}_{0.002}\text{Cr}_{0.001}\text{K}_{0.001})(\text{Si}_{7.932}\text{Al}_{0.083})\text{O}_{22}(\text{OH})_2$. Composition was determined through the average of sixteen spot analyses on three different single crystals. The samples were homogenous with no zoning as evidenced from the electron backscattered image. All iron was assigned as Fe^{2+} to maintain charge balance, however the presence of trace amounts of Fe^{3+} is a possibility. Garnet, chromite, albite, diopside, scapolite, sphene glass and orthoclase standards were used.

The chemical formula was calculated based on 23 O atoms as described by Hawthorne and Oberti (2007). This calculation assumes that $(\text{O},\text{OH},\text{F},\text{Cl}) = 2$ apfu and as no F and Cl were

detected from the microprobe analysis, we assumed that there were 2 apfu of OH. The results from the microprobe analysis are shown in table 2.1.

Ambient-pressure X-ray diffraction

To characterize the ambient pressure crystal structure of the sample used in the high-pressure experiments, a euhedral, platelet crystal, approximately 0.15 x 0.09 x 0.02 mm in size was selected. The crystal was mounted on a Bruker D8 Venture single crystal diffractometer with a Ag I μ S microfocus source (0.56089 Å) and PHOTON-II CPAD detector at the University of Hawaii at Manoa's X-ray Atlas Diffraction Laboratory. The X-ray diffraction data was collected from a θ range of 3.077 to 25.547° with completeness to $\theta = 19.665$. Least-squares structure refinement was done with the program SHELXL (Sheldrick 2008). The initial structure model of grunerite from Finger (1969) was used. All atoms were refined using anisotropic atomic displacement parameters. Full occupancy was assumed for the M1, M2, M3, T1 and T2 sites, based on the calculated chemical formula for our sample. Partial occupancy was refined for the M4 site, which is nominally occupied by Fe²⁺ (Hirschmann et al. 1994) . The A site was assumed to be unoccupied as stoichiometric grunerite has a vacant A site, despite our crystal having a small amount of Na and K, which occupies the A site. The small amount of Na and K in our crystal is equivalent to <0.19 of an electron per unit cell, which is too small of a charge to be detected by the difference-Fourier maps in the structure refinement. The structure was refined using the determined chemical formula from the microprobe analysis as a restraint, however as diffraction experiments cannot resolve small compositional differences, the small amounts of Ti (0.002 apfu) and Cr (0.001 apfu) were ignored. Fe and Mn have similar X-ray atomic scattering factors, and as such, these atoms were grouped together in the refinement. The M1, M2 and M3 sites were only occupied by Mg²⁺ and Fe²⁺, the M4 site was occupied by Fe²⁺ and Ca²⁺ and the T1 and T2 sites

only contained Si. The refinement assumed no substitutional disorder of Mg^{2+} in the M4 site as there is a strong preference for Fe^{2+} and Ca^{2+} in the M4 site (Hirschmann et al. 1994). The determined site occupancies for the four M sites are: M1: $\text{Fe}^{2+} = 0.731(4)$, $\text{Mg}^{2+} = 0.269$; M2: $\text{Fe}^{2+} = 0.560(4)$, $\text{Mg}^{2+} = 0.440$; M3: $\text{Fe}^{2+} = 0.749(6)$, $\text{Mg}^{2+} = 0.251$; M4: $\text{Fe}^{2+} = 0.966(4)$, $\text{Ca}^{2+} = 0.022(4)$. Based on these values our refined chemical formula is $(\text{Fe}_{5.26}\text{Mg}_{1.669}\text{Ca}_{0.044})(\text{Si}_8)\text{O}_{22}(\text{OH})_2$, which is in good agreement with our calculated chemical formula.

High-pressure X-ray diffraction

High-pressure single-crystal X-ray diffraction experiments were performed at beamlines 13BM-C and 13ID-D (GSECARS) of the Advanced Photon Source (APS), Argonne National Laboratory. Three separate experiments were conducted on the natural grunerite sample. Run 1 (13BM-C) consisted of 5 pressure steps ranging from 1.13(2) to 7.4(1) GPa, Run 2 (13ID-D) consisted of 6 pressure steps ranging from 9.0(1) to 25.6(5) GPa and Run 3 (13BM-C) consisted of 3 pressure steps at 10.6(2), 19.2(3) and 22.8(4) GPa. In run 1 we observed the known phase transition from α to β , while in run 2 we observed for the first time the novel phase transition from β to γ . Run 3 was used to solve the new γ -grunerite phase. We utilized data from three different runs as there was not enough coverage of reciprocal space in run 2 to solve the new structure. All experiments were conducted at 298 K.

Two crystals of grunerite with approximate size of 0.065 x 0.030 x 0.005 mm were loaded into a 4-pin diamond-anvil cell (DAC) with 400 μm culet diamonds. Each run utilized a different pair of crystals, however all crystals used in this study came from the same bulk sample. Conical anvils and backing plates (Boehler and De Hantsetters 2004) were used in runs 1 and 3 to increase coverage of reciprocal space. For run 2, standard brilliant cut diamonds anvils with 0.300 mm culets were used on asymmetric backing plates (cubic boron nitride seat towards the X-ray source

and tungsten carbide toward the detector). A hole, 0.210 mm in diameter, was drilled through a 0.250 mm thick rhenium gasket that was preindented to 0.040 mm to act as the sample chamber. Two small ruby spheres were placed in the sample chamber together with the sample crystals as a pressure calibrant. Pressure was calculated from the shift of the R1 ruby fluorescence line (Dewaele et al. 2008). The DAC was gas loaded at the GSECARS-COMPRES facility (Rivers et al. 2008) with neon as the pressure medium to ~ 1.37 GPa. After gas loading the sample chamber had shrunk to ~ 0.115 mm in diameter. Ruby fluorescence spectra were measured at each pressure point both before and after the X-ray data collection. Uncertainties in pressures were taken as 2% of the pressure measurement.

High-pressure diffraction experiments conducted at experimental station 13BM-C were performed using a monochromatic X-ray beam with energy of 28.6 keV (0.434 Å), and 1 eV bandwidth, focused with a Kirkpatrick-Baez mirror system to a spot of 0.015 mm x 0.015 mm, measured as full width at half maximum (FWHM). The MAR165 charge-coupled device (CCD) detector was placed roughly 180 mm away from the sample, and ambient LaB₆ powder was used to calibrate the distance and tilting of the detector. The sample was placed at the rotation center of the diffractometer and aligned using an optical microscope. A total angular range from $\varphi = 56^\circ$ to 125° (total angular opening of $\pm 34.5^\circ$) was covered during the scans. A series of step and wide-step φ -exposures were collected. Step scans involved 1° angular increments, while wide-step scans had 9.8° angular increments. The exposure time was at 3 sec/ $^\circ$. After collection of step and wide-step φ -exposures at the zero detector position, more wide-step φ -exposures were recorded with the detector rotated about its horizontal axis (2θ) by 20° and then with the detector rotated about the vertical axis (ν) by 10° and -10° . Exposure time for the non-zero detector position was at 6 sec/ $^\circ$.

The monochromatic diffraction experiment at 13ID-D was conducted in a similar manner to those performed at 13-BM-C. X-rays with wavelength of 0.295 Å (42 keV) were used with a focused X-ray beam size of 0.003 mm x 0.003 mm. Diffraction images were collected using a MAR165 charge coupled device (CCD) detector, placed at a sample-to detector distance of approximately 200 mm. The total rotation range around the vertical axis of the instrument (ω) was $\pm 22^\circ$, with step scans covering 1° width and exposure time at 0.5 sec/ $^\circ$.

Step φ -exposures (13BM-C) and ω -scans (13ID-D) were used in reconstruction of the crystal's reciprocal lattice to determine the unit cell parameters and to index the diffraction pattern. Wide-step φ -exposures and ω -scans were used to determine d-spacings, azimuthal angles around the beam center and peak intensities of each diffraction peak in order to solve the crystal structure. Data collection was performed following the procedure described by (Dera 2007; Dera et al. 2013b) and data was analyzed using the GSE_ADA/RSV program. Integrated peak intensities were corrected for Lorenz, polarization, DAC absorption and sample displacement effects using the methods implemented in GSE_ADA. Because of the high incident energy, low absorption coefficient and negligible sample thickness the effects of sample absorption were ignored. The structure of the β -phase was refined using an initial cummingtonite model from Yang et al. (1998). The structure of the new high-pressure γ -phase at 22.8(4) GPa was solved using the initial ambient pressure model from Finger (1969). Least-squares structure refinement for selected pressures was done with the program SHELXL (Sheldrick 2008). The procedure for refinement of the high-pressure data was similar to the ambient pressure data, however, all atoms in the high-pressure data were refined with isotropic ADPs due to limited coverage of reciprocal space. The site occupancies of all the high-pressure refinements were constrained to those determined from the ambient structure refinement. In some of the high-pressure data we were unable to locate hydrogen

atoms, in order to keep the refinements consistent, we have opted to have all hydrogen atoms omitted from the high-pressure structural refinement. Details of the crystal structure refinement, unit cell parameters at each pressure, refined fractional coordinates for all the atoms, bond lengths and atomic displacement parameters for selected pressures are given in tables 2.2 – 2.5. Unfortunately, only one pressure point of the new high-pressure phase produced data allowing to solve and refine the structure, due to limited coverage of reciprocal space owing to the high-pressure apparatus.

2.3 Results and Discussion

Phase transition in grunerite

Three different phases were observed in grunerite on compression to 25.6(5) GPa. A comparison of all three structures is shown in figure 2.1. The previously reported $C2/m$ (α) – $P2_1/m$ (β) transition was observed between 5.2(1) and 7.4(1) GPa and another transformation was detected between 16.3(3) to 19.2(3) GPa. Unit cell parameters of grunerite up to 25.6(5) GPa are listed in table 2.3. The new phase transition transformed the symmetry from $P2_1/m$ (β) to a previously unreported structure. This new structure has monoclinic space group $C2/m$ (γ), determined through analysis of systematic absences in the diffraction pattern and, as evidenced through structure solution and refinement. The structure of all 3 phases have been solved and refined (table 2.2).

At 7.4(1) GPa, the observed structure adopts a primitive lattice based on reflections violating the $C2/m$ space group. The α – β phase transition is thus expected to occur between 5.2(1) and 7.4(1) GPa for the studied sample. The examined crystal transformed to the $P2_1/m$ β -phase by 7.4(1) GPa. There is a small slope change in a , b , c and β at the $C2/m$ - $P2_1/m$ transition (figure 2.2). In all four unit cell parameters the slope has decreased suggesting a change in the compression

mechanism. Yang et al. (1998) estimated that the $C2/m$ - $P2_1/m$ transition pressure has a linear dependence on X_{Fe} with the relationship $P_{\text{tr}} = -1.23 + 4.52 X_{\text{Fe}}$. Based on this linear dependence, our sample would be expected to transform to β -grunerite at ~ 2.21 GPa, which is much lower than our reported value. This suggests that the $\alpha - \beta$ phase transition pressure is affected by other factors in addition to X_{Fe} .

At 19.2(3) GPa, the structure adopts a C-centered lattice again, as determined through analysis of systematic absences in the diffraction pattern. A similar high-pressure phase was previously indicated in a synthetic amphibole with composition $\text{Na}(\text{NaMg})\text{Mg}_5\text{Si}_8\text{O}_{22}(\text{OH})_2$ by infrared spectroscopy experiments (Iezzi et al. 2006), based on the presence of a single OH-stretching band. However, until now there have been no previous diffraction experiments reported to confirm this and constrain the crystal structure. This new phase adopts a monoclinic structure with space group $C2/m$, with unit cell parameters at 22.8(4) GPa, $a = 9.287(6)$ Å, $b = 17.203(1)$ Å, $c = 4.89(1)$ Å, $\beta = 107.99(1)^\circ$ and $V = 744.4(5)$ Å³. The $\beta - \gamma$ phase transition in grunerite is accompanied by a discontinuous increase in the a unit cell parameter and β angle (figure 2.2). The a unit cell parameter of β -grunerite at 16.3(3) GPa is 8.956(8) Å and in γ -grunerite at 19.2(3) GPa it increases to 9.34(1) Å. Furthermore, β increases from $103.36(2)^\circ$ to $107.52(1)^\circ$ across the transition. Sueno et al. (1973) defined the tetrahedral displacement parameter ‘d’, as the distance between the centers of two opposing six-membered tetrahedral rings, and found a negative linear correlation between d and β . Figure 2.3 shows a plot of calculated d values against β , and confirms this negative linear relationship. Whittaker (1960) has associated the degree of the closest packing of the tetrahedral chains with an increase in β , which follows directly from Prewitt and Down’s 8th rule of thumb on high pressure effects on bonding and coordination number (Prewitt and Downs 1998), that high-pressure structures tend to be composed of closest-packed arrays of atoms.

Equation of state, bulk moduli and linear compressibilities

Weighted volume and pressure data from all three phases were used to fit the second-order Birch-Murnaghan (BM) equation of state (EOS) using the program EOS-FIT V7 program (Gonzalez-Platas et al. 2016). The results of the EOS are plotted in figure 2.4 and shown in table 2.6. The bulk moduli determined from this study is in good agreement with Yang et al. (1998), the larger V_0 in our study is likely due to greater Fe content in our sample (ionic radius of $^{VI}\text{Mg}^{2+} = 0.72 \text{ \AA}$ and high spin $^{VI}\text{Fe}^{2+} = 0.78 \text{ \AA}$ (Shannon 1976)).

Linear compressibilities, defined as $\beta_{10} = 1/3K_{10}$ (Angel 2000), were determined by weighted least-squares fit of the linearized second-order BM equation of state (figure 2.2 and table 2.6). Linear compressibilities for α -grunerite are 0.0052(1), 0.0035(1) and 0.0038(1) GPa^{-1} for β_a , β_b and β_c respectively, with a ratio of 1.49:1.00:1.10. For the $P2_1/m$ polymorph the axial compressibilities were 0.007(1), 0.0038(3) and 0.00381(2) GPa^{-1} for β_a , β_b and β_c respectively, with a ratio of 1.86:1.00:0.99. Zhang et al. (1992) reported $\beta_a:\beta_b:\beta_c$ of 1.42:1.00:1.03 for a single-crystal X-ray study on natural grunerite up to 5.1 GPa, which is in good agreement with our reported values for the ambient phase. For the new high-pressure γ -phase the linear compressibilities were 0.0023(4), 0.0040(8) and 0.005(1) GPa^{-1} for β_a , β_b and β_c respectively, with a ratio of 0.56:1.00:1.41. All three phases display strong compressional anisotropy. In the ambient pressure and $P2_1/m$ phase the a axis is the most compressible while the b and c axis display similar compressibilities. In the new high-pressure γ -phase the a axis is the least compressible while the most compressible direction is along the crystallographic c axis indicating a change in the compression mechanism. It should be noted that the degree of compressional anisotropy increases with each phase transition.

Structural changes with pressure

The kinking angle of the silicate chains are characterized by the O5-O6-O5 angle. With increasing pressure, the kinking angle in α -grunerite decreases from $171.3(1)^\circ$ at ambient pressure to $168(3)^\circ$ at $5.2(1)$ GPa. During the α - β phase transition, the silicate chain becomes two crystallographically unique chains, the A and B chain. Upon further compression, the A and B chain kinking angle decreases. The A chain kinking angle decreases from $166(4)^\circ$ at $7.4(1)$ GPa to $157(1)^\circ$ at $16.3(3)$ GPa, while in the B chain it decreases from $146(4)^\circ$ to $141(1)^\circ$ at the same respective pressures. The difference between the kinking angle of the two chains ($\Delta\theta$) decreases from $19.8(5)^\circ$ to $16.0(5)^\circ$ from $7.4(1)$ to $16.3(3)$ GPa. During compression the sense of rotation of both A and B chains remain the same, the A chain being S-rotated and the B chain O-rotated. The change in rotation type in the A chain to S-type parallels the clinopyroxene $C2/c$ to $P2_1/c$ transition where the A chain is also S-rotated and more extended than the B chain, which is O-rotated and significantly more kinked (Hugh-Jones et al. 1994). Yang et al. (1998) observed a change in the sense of rotation in the A chain from O to S-rotated with increasing pressure, however our results show that the A-chain remains S-rotated throughout. In the new γ -phase of grunerite, the A and B chain consequently become one distinct chain because of the change in symmetry, geometrically they are both equal to the B chain in the β -phase. Similarly, to the α -phase, the silicate chains in the high-pressure γ -phase are also O-rotated. Of more importance however, is the change in the kinking angle, which at $22.8(4)$ GPa is $137.5(4)^\circ$.

In clinopyroxenes the HT $C2/c$ structure is characterized by chains that are nearly fully extended, whereas the HP $C2/c$ phase displays tetrahedral chains that are more kinked (Arlt et al. 2000; Yang and Prewitt 2000; Tribaudino et al. 2001; Tribaudino et al. 2003). Correspondingly to the structural changes observed in pyroxenes, the low-pressure $C2/m$ α -grunerite is

characterized by silicate chains which are slightly bent from being fully extended ($171.3(1)^\circ$ at ambient pressure), while the high-pressure $C2/m$ γ -grunerite has silicate chains that display more kinking ($137.5(4)^\circ$ at $22.8(4)$ GPa). The primitive lattice, β -grunerite phase, is an intermediate structure having two silicate chains displaying different behavior from both the low and high-pressure C-centered polymorphs. The structural evolution of the double silicate chains is shown in figure 2.1. It is interesting to note, as discussed by Papike and Ross (1970), that with further kinking towards the maximum angle of 120° the hexads of SiO_4 tetrahedra will possess 3-fold rotation symmetry. Complete O-rotation of the double chains will result in a cubic close packing of oxygen atoms. In the HP $C2/c$ clinopyroxene structure, oxygen atoms also display behavior near that of cubic closest-packing due to the extreme kinking of the silicate chains. While the degree of closest packing in amphiboles can be characterized by an increase in the monoclinic β angle this is not the case for clinopyroxenes. In previous high-pressure experiments on clinopyroxenes, the monoclinic β angle decreases with pressure and has a discontinuous decrease across the $P2_1/c$ to HP $C2/c$ phase transition (Hugh-Jones et al. 1994; Arlt et al. 1998; Tribaudino et al. 2001; Alvaro et al. 2010), this is in contrast with our study where the β angle increases with pressure.

Yang et al. (1998) discussed the correlation between the variation of O5-O6-O5 angle and changes in M4-O5 and M4-O6 distances due to the $C2/m$ - $P2_1/m$ phase transition in cummingtonite. The values for M4-O5 and M4-O6 distances are shown in figures 2.6 and 2.7. Our study is in good agreement with these observations. In the $P2_1/m$ β -phase, the M4-O5A distance increases with pressure from $3.50(4)$ Å at $7.4(1)$ GPa to $3.70(2)$ Å at $16.3(3)$ GPa, while the M4-O5B distance decreases across the same pressure range from $2.54(5)$ Å to $2.31(2)$ Å. This is due to the increase in coordination from six to seven in the M4 site as the structure transitions from the α -phase to the β -phase. The kinking of the silicate chain pushes the O5B atom to coordinate with M4 while O5A

moves further away. With increasing pressure as the structure changes from $P2_1/m$ to the high-pressure $C2/m$ γ -phase the M4-O6 distance is significantly increased to 3.00(1) Å due to further kinking of the tetrahedral chains. The coordination number in M4 decreases to six across the phase transition, as the O6 atom moves further away from the coordination sphere, whereas the O5 atom moves closer in (figure 2.8). In the α -phase the M4 shares five edges with surrounding polyhedra (figure 2.9). Two edges are shared with the M2 polyhedra, one edge with the M1 polyhedron and two edges with T2 polyhedra. In the β -phase the M4 shares an additional edge with the T2A tetrahedron, decreasing the stability of the ionic structure due to the increase in cation-cation repulsion as per Pauling's third rule. During the β - γ phase transition, as the M4 coordination number decreases back to six, the stability of the polyhedral configuration increases, as the number of shared edges decreases from six in β -grunerite, to three in γ -grunerite. In the γ -phase, the M4 polyhedron shares two edges with the M2 polyhedra and one edge with the M1 polyhedron. As the M4 site in amphiboles are considerably more distorted than the M1, M2 and M3 sites and are generally filled with relatively larger cations, it is appropriate to compare them to the M2 polyhedron in pyroxenes, which also displays similar properties. In the HP $C2/c$ clinopyroxene phase, the extreme kinking of the silicate-chain involves breaking of bonds between O3 and M2 atoms, as a consequence, the M2 site no longer shares any edges with the silicate chain (Hugh-Jones et al. 1994; Downs 2003). In a similar manner, in γ -grunerite the extreme kinking of the double silicate chains leads to no sharing of edges between the SiO_4 tetrahedra and the M4 polyhedron.

2.4 Implications

The close similarities of the physical, chemical and crystallographic properties between amphiboles and pyroxenes have been known for quite some time (Warren 1930; Warren and Modell 1930b). Carpenter (1982) determined that the high-temperature to low-temperature displacive transformations in amphiboles and pyroxenes to be exactly analogous, even in the resulting microstructures. The non-ambient behavior of clinopyroxenes have been well studied across a wide variety of compositions (Brown et al. 1972; Smyth 1974; Hugh-Jones et al. 1994; Arlt and Armbruster 1997; Arlt et al. 1998; Arlt et al. 2000; Yang and Prewitt 2000; Tribaudino et al. 2001; Tribaudino et al. 2003; Nestola et al. 2008; Alvaro et al. 2010). These studies have shown that clinopyroxenes undergo a series of phase transformations from the high-temperature- $C2/c$ to $P2_1/c$ to high-pressure- $C2/c$ phase. Based on their comparable behavior, a similar series of phase transitions is expected in clinoamphiboles. Our single-crystal experimental data have shown the existence of a new phase of grunerite above 19.2(3) GPa. This study is the first structural report to show the existence of three polymorphs within an amphibole group mineral, which closely mirrors the phase transition sequence in clinopyroxenes as mentioned above. The existence of the γ -phase of grunerite illustrates the corresponding structural relations and demonstrates that the parallel phase transformation behavior is not only limited to temperature as proposed by Carpenter (1982), but also includes pressure. The high-temperature- $C2/c$ to $P2_1/c$ to high-pressure- $C2/c$ transformations in clinopyroxenes (Arlt et al. 2000; Nestola et al. 2008) is analogous to the α to β to γ -phase transition seen in this study. It is worth mentioning that in both clinopyroxenes and clinoamphiboles, high-pressure and high-temperature phase transitions have the same space group and both phases are isometric to each other (Tribaudino et al. 2001; Tribaudino et al. 2003).

Equilibrium phase transformation sequences and chemical reactions experienced by the major rock forming minerals have been extensively studied and are well understood. Metastable transformations however are poorly constrained. Constraining the stability of these metastable phases is important, as they may have significant geophysical implications as suggested by Agrusta et al. (2014) and Tetzlaff and Schmeling (2000) for both olivine and pyroxene in subducting slabs. In the case of both these minerals, metastability promotes slab stagnation within the mantle transition zone due to the low-density metastable phases, which provide positive buoyancy effects (Agrusta et al. 2014). The density of grunerite, clinoferrosilite (Solomatova et al. 2018) and PREM (Dziewonski and Anderson 1981) are shown in figure 2.10. The effects of thermal expansion have been ignored in both grunerite and clinoferrosilite as there has been no reported thermal expansion data for grunerite. Clinoferrosilite is the Fe end-member pyroxene and is the single-chain analog of grunerite. Ferrosilite is likely to be part of the stable phase assemblage during equilibrium phase transformations of grunerite. The density of clinoferrosilite is approximately 16% greater than that of grunerite, as we have neglected the thermal expansion in both these calculations this comparison is consistent. Agrusta et al. (2014) has demonstrated through geodynamic modelling that the metastable preservation of pyroxene has a strong potential for affecting slab stagnation. As grunerite would react to form denser phases such as ferrosilite, it is likely that the metastable preservation of this phase would deliver a positive buoyancy effect and thus could contribute to slab stagnation. It is conceivable that this metastable phase of grunerite would exist in geologic environments such as the Tonga slab, where the thermal profile is lower than the mantle adiabat (Ganguly et al. 2009). It is estimated that the temperature of the Tonga slab within the mantle transition zone is less than 900°C (Ganguly et al. 2009). The high-pressure and anomalously cold-temperature of this region may be a likely geologic environment where

metastable amphiboles like γ -grunerite are preserved. The temperature in this region is near the upper limit of amphibole stability before dehydration occurs (Wallace and Green 1991; Welch and Graham 1992; Konzett et al. 1997; Ernst and Liu 1998; Niida and Green 1999; Fumagalli and Poli 2005). The high-pressure, however, may have an effect of increasing the dehydration temperature. Constraining the stability of this metastable phase is important as it may have significant geophysical and petrological consequences, since amphiboles are commonly used as petrogenetic indicators and in geodynamic modelling. Phases similar to γ -grunerite may exist for other clino- and orthoamphiboles of different composition, therefore further high-pressure investigations of these systems should be encouraged. In addition, simultaneous high-temperature and high-pressure studies on grunerite are needed to constrain the stability of γ -grunerite and to determine the dehydration temperature of this phase.

2.5 Tables and Figures

Table 2.1. Results from microprobe analyses

Constituent	Wt.%	Range	Stand. dev.	Probe standard*	Crystal	Ions/formula
FeO	39.14	38.06 – 39.9	0.52	Garnet, Verma (Mn)	LiF	5.237
MgO	6.9	6.47 – 7.21	0.28	Chromite USNM 117075	TAP	1.646
Na ₂ O	0.05	0.02 – 0.1	0.02	Albite, Amelia	TAP	0.015
Al ₂ O ₃	0.44	0.34 – 0.6	0.07	Chromite USNM 117075	TAP	0.083
SiO ₂	49.58	49.15 – 49.93	0.22	Albite, Amelia	TAP	7.932
CaO	0.36	0.28 – 0.47	0.05	Diopside-2 (UCLA)	PETH	0.061
MnO	0.38	0.31-0.49	0.05	Garnet, Verma (Mn)	LiF	0.051
Cl	0	0 – 0.02	0.01	Scapolite	PETH	0
TiO ₂	0.02	0 – 0.05	0.02	Sphene glass	LiFH	0.002
K ₂ O	0.01	0 – 0.02	0.01	Orthoclase (OR-1)	PETH	0.001
Cr ₂ O ₃	0.01	0 – 0.02	0.01	Chromite USNM 117075	LiFH	0.001
Total	96.8					

* Probe standard compositions (Wt.%)

Garnet, Verma (Mn) = SiO₂: 36.88, Al₂O₃: 20.82, FeO: 18.04, CaO: 0.24, MnO: 24.6

Chromite USNM 117075 = Al₂O₃: 9.92, FeO: 13.04, MgO: 15.2, MnO: 0.1, TiO₂: 0.12, Cr₂O₃: 60.5, NiO: 0.16, U₂O₃: 0.09

Albite, Amelia = SiO₂: 68.75, Al₂O₃: 19.43, Fe₂O₃: 0.02, Na₂O: 11.7, K₂O: 0.1

Diopside-2 (UCLA) = SiO₂: 55.27, Al₂O₃: 0.05, FeO: 0.94, MgO: 18.29, CaO: 25.47, MnO: 0.1, Na₂O: 0.05, TiO₂: 0.06

Scapolite = SiO₂: 49.78, Al₂O₃: 25.05, FeO: 0.17, CaO: 13.58, Na₂O: 5.2, K₂O: 0.94, Cl: 1.43, CO₂: 2.5, SO₃: 1.32, H₂O⁺: 0.21

Sphene glass: SiO₂: 30.65, CaO: 28.6, TiO₂: 40.75

Orthoclase (OR-1): SiO₂: 64.39, Al₂O₃: 18.58, FeO: 0.03, Na₂O: 1.14, K₂O: 14.92, BaO: 0.82, SrO: 0.035, NiO: 0.03, U₂O₃: 0.08, SO₃: 0.03, H₂O⁺: 0.08

Table 2.2. Representative single-crystal structure refinement for grunerite at selected pressures

Run No.	0	1	3	3
Beamline	-	13BM-C	13BM-C	13BM-C
Wavelength (Å)	0.560	0.434	0.434	0.434
Pressure (GPa)	0	1.13(2)	10.6(2)	22.8(4)
Temperature (K)	298	298	298	298
θ range for data collection	3.077 – 25.547	1.501 – 19.542	1.401 – 13.796	1.446 – 23.182
No. of reflections collected	7782	920	669	2466
No. of independent reflections	1795	258	287	257
Reflections violating $C2/m$ S.G.			338	
No. of parameters refined	103	42	84	42
Limiting indices	$-14 \leq h \leq 14$ $-28 \leq k \leq 28$ $-8 \leq l \leq 5$	$-14 \leq h \leq 8$ $-8 \leq k \leq 7$ $-6 \leq l \leq 6$	$-4 \leq h \leq 4$ $-19 \leq k \leq 18$ $-5 \leq l \leq 5$	$-6 \leq h \leq 6$ $-24 \leq k \leq 24$ $-7 \leq l \leq 7$
Space group	$C2/m$	$C2/m$	$P2_1/m$	$C2/m$
R_{int}	0.0672	0.0611	0.0682	0.1218
Goodness of Fit	1.083	1.109	1.139	1.267
wR_2	0.0928	0.1204	0.1587	0.2406
R_1	0.0382	0.0432	0.0592	0.0998

Table 2.3. Unit cell parameters of grunerite at various pressures

Run	Pressure (GPa)	a (Å)	b (Å)	c (Å)	β (°)	V (Å ³)	Space group
0	0	9.553(1)	18.327(2)	5.3382(8)	101.854(4)	914.74(8)	$C2/m$
1	1.13(2)	9.504(1)	18.24(1)	5.3224(8)	102.04(1)	902.6(8)	$C2/m$
1	2.22(4)	9.445(1)	18.18(1)	5.3097(7)	102.38(1)	891.0(8)	$C2/m$
1	3.63(7)	9.390(1)	18.11(1)	5.2765(8)	102.63(1)	875.8(9)	$C2/m$
1	5.2(1)	9.338(1)	18.03(1)	5.2510(9)	102.86(1)	862.0(8)	$C2/m$
1	7.4(1)	9.261(1)	17.92(1)	5.2196(8)	103.04(1)	844.2(9)	$P2_1/m$
2	9.0(1)	9.226(4)	17.804(1)	5.1898(3)	103.15(1)	830.1(3)	$P2_1/m$
3	10.6(2)	9.18(1)	17.751(2)	5.1694(7)	103.13(2)	820.8(5)	$P2_1/m$
2	12.0(2)	9.107(6)	17.689(2)	5.1524(4)	103.34(2)	807.7(4)	$P2_1/m$
2	16.3(3)	8.956(8)	17.497(2)	5.1040(5)	103.36(2)	778.2(5)	$P2_1/m$
3	19.2(3)	9.332(1)	17.326(2)	4.9456(8)	107.52(3)	762.5(9)	$C2/m$
2	20.6(4)	9.31(1)	17.298(5)	4.9210(9)	108.03(4)	753(1)	$C2/m$
3	22.8(4)	9.287(6)	17.203(1)	4.8989(4)	107.99(1)	744.3(5)	$C2/m$
2	23.0(4)	9.277(9)	17.1759(3)	4.8934(6)	108.25(3)	740.5(8)	$C2/m$
2	25.6(5)	9.243(9)	17.127(4)	4.8706(6)	108.63(3)	730.7(8)	$C2/m$

Table 2.4. Atomic positional coordinates and atomic isotropic displacement parameters

Pressure (GPa)	Atom	x	y	z	U_{eq}
1.13(2)	M1	0	0.0876(3)	0.5	0.010(1)
	M2	0	0.1778(4)	0	0.010(1)
	M3	0	0	0	0.009(1)
	M4	0	0.2578(3)	0.5	0.010(1)
	Si1	0.2887(2)	0.0836(4)	0.2736(5)	0.006(1)
	Si2	0.2993(2)	0.1680(4)	0.7783(5)	0.006(1)
	O1	0.1151(5)	0.0882(8)	0.208(1)	0.008(1)
	O2	0.1250(5)	0.1718(8)	0.715(1)	0.007(1)
	O3	0.1157(8)	0	0.705(1)	0.009(2)
	O4	0.3824(6)	0.243(1)	0.767(1)	0.013(1)
	O5	0.3512(5)	0.130(1)	0.064(1)	0.011(1)
	O6	0.3513(5)	0.1174(8)	0.558(1)	0.010(1)
	O7	0.3418(9)	0	0.268(1)	0.013(2)
	10.6(2)	M1	-0.2535(1)	0.3355(1)	0.4687(7)
M2		-0.252(1)	0.4257(2)	0.9697(7)	0.011(1)
M3		-0.251(1)	0.25	0.9702(9)	0.010(1)
M4		-0.2604(8)	0.5101(2)	0.4605(6)	0.012(1)
Si1A		0.044(3)	0.3341(3)	0.248(1)	0.007(2)
Si1B		0.547(2)	0.8318(3)	0.314(1)	0.009(2)
Si2A		0.040(3)	0.4207(3)	0.750(1)	0.011(2)
Si2B		0.558(2)	0.9152(3)	0.819(1)	0.009(2)
O1A		-0.136(6)	0.3357(6)	0.178(3)	0.013(5)
O1B		0.362(5)	0.8355(6)	0.234(3)	0.016(4)
O2A		-0.131(6)	0.4211(7)	0.685(3)	0.018(5)
O2B		0.370(5)	0.9201(6)	0.745(3)	0.013(4)
O3A		-0.115(6)	0.25	0.691(4)	0.014(5)
O3B		0.373(5)	0.75	0.735(3)	0.004(4)
O4A		0.122(3)	0.5015(6)	0.789(2)	0.005(3)
O4B		0.631(4)	0.9907(6)	0.750(2)	0.011(3)
O5A		0.117(4)	0.3662(6)	0.010(3)	0.015(4)
O5B	0.616(4)	0.8948(6)	0.139(2)	0.009(3)	
O6A	0.117(4)	0.3855(6)	0.512(2)	0.014(3)	
O6B	0.608(5)	0.8513(6)	0.630(3)	0.013(3)	
O7A	0.104(6)	0.25	0.305(3)	0.013(5)	
O7B	0.611(6)	0.75	0.260(3)	0.009(5)	
22.8(4)	M1	0	0.0857(2)	0.5	0.005(1)
	M2	0	0.1747(2)	0	0.004(1)
	M3	0	0	0	0.006(1)
	M4	0	0.2638(2)	0.5	0.007(1)
	Si1	0.307(1)	0.0822(2)	0.340(1)	0.006(1)
	Si2	0.301(1)	0.1681(2)	0.833(1)	0.004(1)
	O1	0.135(4)	0.0861(5)	0.236(3)	0.004(3)
	O2	0.121(4)	0.1724(5)	0.735(3)	0.008(3)
	O3	0.139(5)	0	0.738(4)	0.002(3)
	O4	0.380(4)	0.2439(5)	0.759(3)	0.010(2)
	O5	0.363(3)	0.1499(4)	0.184(3)	0.006(2)
	O6	0.368(3)	0.0946(5)	0.690(3)	0.009(3)
	O7	0.363(5)	0	0.267(4)	0.009(3)

Table 2.5. Bond lengths (Å) for grunerite at selected pressures

Pressure (GPa)	1.13(2)	10.6(2)	22.8(4)	
		Set A	Set B	
M1-O1	2.075(6)	2.04(3)	2.01(3)	2.06(3)
M1-O2	2.12(1)	2.06(3)	2.02(2)	2.00(2)
M1-O3	2.112(7)	2.14(3)	2.02(2)	2.07(3)
Average	2.10233	2.04833		2.04333
M2-O1	2.14(1)	2.08(3)	2.05(2)	2.08(2)
M2-O2	2.111(5)	2.04(3)	2.03(3)	1.96(2)
M2-O4	2.06(1)	1.99(2)	2.03(2)	1.94(1)
Average	2.10367	2.03667		1.99333
M3-O1	2.12(1)	2.02(3)	1.99(2)	2.05(2)
M3-O3	2.093(8)	2.12(4)	2.08(3)	2.08(3)
Average	2.1065	2.0525		2.065
M4-O2	2.15(1)	2.15(3)	2.05(3)	2.06(2)
M4-O4	1.985(5)	2.02(2)	1.98(2)	1.94(2)
M4-O5			2.45(1)	2.23(1)
M4-O6	2.73(1)	2.26(2)	2.96(2)	
Average	2.28833	2.26714		2.07667
T1-O1	1.616(6)	1.61(4)	1.66(4)	1.53(4)
T1-O5	1.61(1)	1.63(2)	1.65(2)	1.56(1)
T1-O6	1.631(9)	1.64(1)	1.63(1)	1.64(1)
T1-O7	1.608(7)	1.59(1)	1.61(2)	1.58(1)
Average	1.61625	1.6175	1.6375	1.5775
T2-O2	1.622(6)	1.53(4)	1.68(4)	1.60(4)
T2-O4	1.59(1)	1.61(2)	1.58(2)	1.58(1)
T2-O5	1.64(1)	1.67(2)	1.66(1)	1.66(1)
T2-O6	1.64(1)	1.68(2)	1.63(2)	1.65(1)
Average	1.623	1.6225	1.6375	1.6225

Table 2.6. Equation of state data for grunerite

Reference	Phase	Pressure medium	P_{\max} (GPa)	K_{0T} (GPa)	K'_{0T}	β_a	β_b	β_c	$\beta_a: \beta_b: \beta_c$
Zhang et al. (1992)	$C2/m$	4:1 meth-eth	5.1	50(1)	13(1)	0.00497(6)	0.00350(4)	0.0062(5)	1.41:1.00:1.03
Yang et al. (1998)	$C2/m$	4:1 meth-eth	7.9	78(3)	4	0.0068(2)	0.0024(3)	0.0028(1)	2.83:1.00:1.17
Yang et al. (1998)	$P2_1/m$	4:1 meth-eth	7.9	71(1)	6.1(5)	0.0043(3)	0.0029(1)	0.0030(1)	1.48:1.00:1.03
This study	$C2/m$	Ne	25.6(5)	78(1)	4	0.0052(1)	0.0035(1)	0.0038(1)	1.49:1.00:1.10
This study	$P2_1/m$	Ne	25.6(5)	66(4)	4	0.007(1)	0.0038(3)	0.00381(2)	1.86:1.00:0.99
This study	$C2/m$	Ne	25.6(5)	66(13)	4	0.0023(4)	0.0040(8)	0.005(1)	0.56:1.00:1.41

Composition:

Zhang et al. (1992) – $(\text{Fe}^{2+}_{5.33}\text{Mg}_{1.46}\text{Fe}^{3+}_{0.14}\text{Na}_{0.05}\text{K}_{0.01}\text{Al}_{0.01})(\text{Si}_{7.92}\text{Al}_{0.08})\text{O}_{22}(\text{OH}_{1.92}\text{F}_{0.05}\text{Cl}_{0.01})$ Yang et al. (1998) – $(\text{Fe}_{3.272}\text{Mg}_{3.445}\text{Ca}_{0.076}\text{Mn}_{0.199}\text{Al}_{0.008})(\text{Si}_{7.983}\text{Al}_{0.017})\text{O}_{22}(\text{OH})_2$ This study - $(\text{Fe}_{5.237}\text{Mg}_{1.646}\text{Ca}_{0.061}\text{Mn}_{0.051}\text{Na}_{0.015}\text{Ti}_{0.002}\text{Cr}_{0.001}\text{K}_{0.001})(\text{Si}_{7.932}\text{Al}_{0.083})\text{O}_{22}(\text{OH})_2$

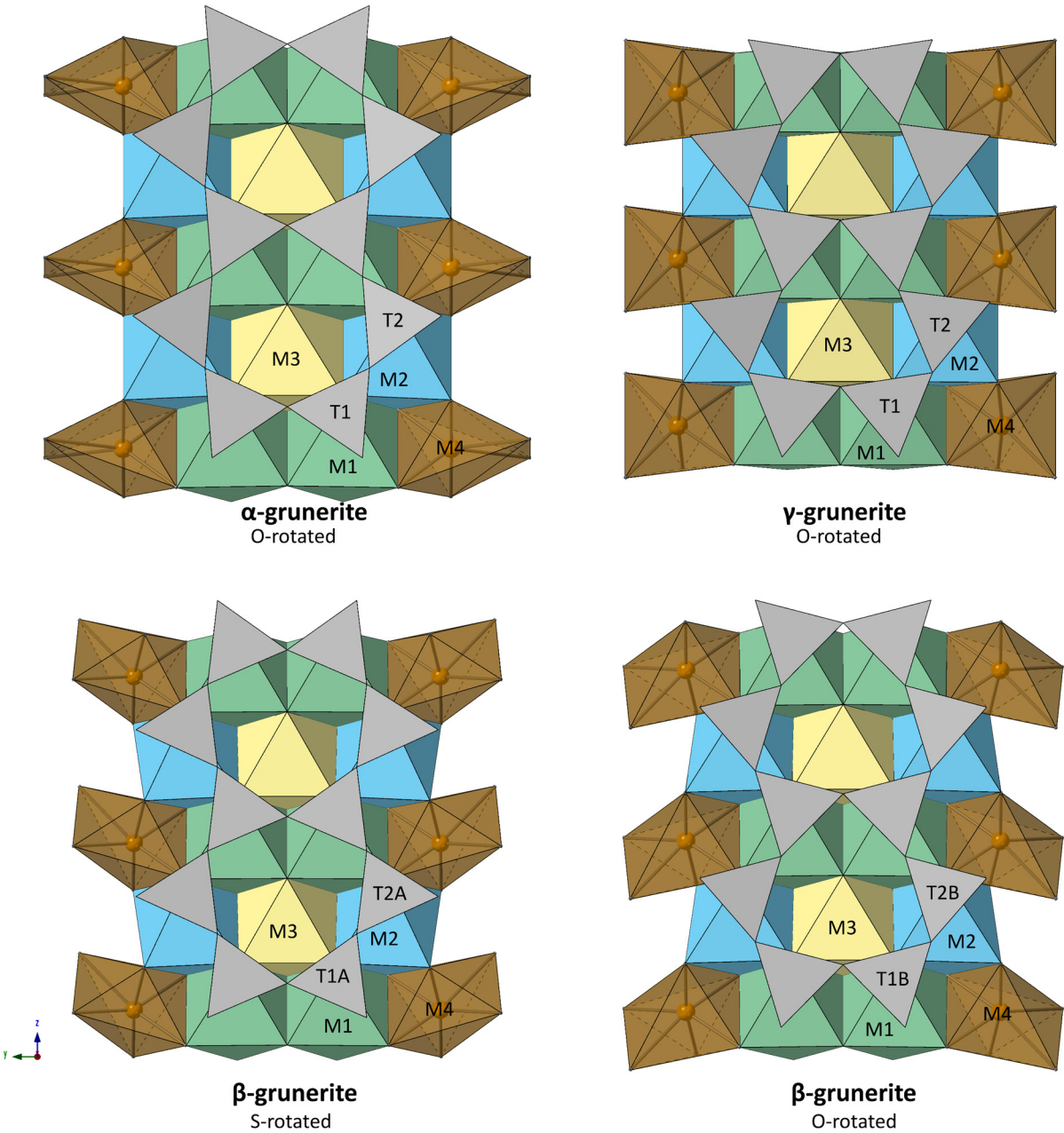


Figure 2.1. (100) projection of the partial structure of grunerite showing the structural changes across the $\alpha - \beta - \gamma$ phase transition. In the α and γ phase the double-chain of tetrahedra are O-rotated. In the β -grunerite phase, the reduction in symmetry causes the double-chains to split into two crystallographically distinct chains, the A-chain (S-rotated) and the B-chain (O-rotated).

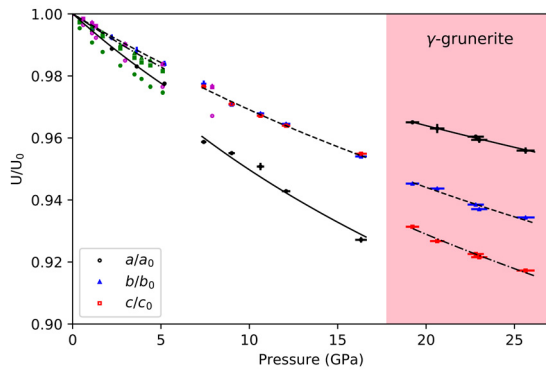


Figure 2.2. Normalized unit cell parameters of grunerite from this study (black, blue and red) plotted against pressure. Results from previous experiments are shown in green (Zhang et al. 1992) and magenta (Yang et al. 1998). Results of linearized second order BM EOS fit for each axis are shown with solid, dash-dot and dashed lines for a/a_0 (in black), b/b_0 (in blue), c/c_0 (in red), respectively.

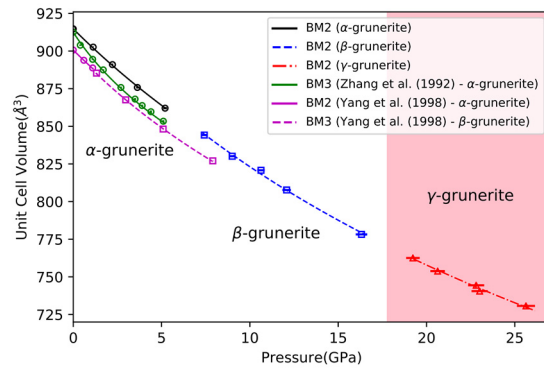


Figure 2.4. Unit cell volume of grunerite from this study (black, blue and red), with a second-order BM EOS, compared to previous experiments (green and magenta, Zhang et al. (1992) and Yang et al. (1998), respectively). Circles, squares and triangles are the ambient pressure α -phase, β -phase and high-pressure γ -phase, respectively.

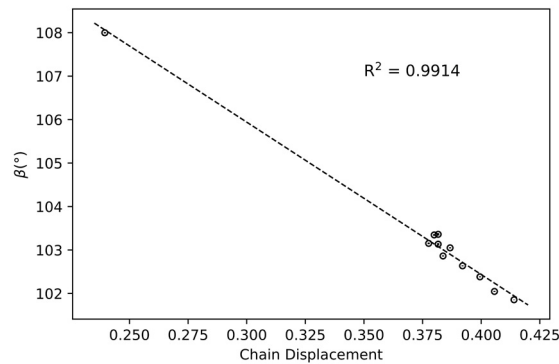


Figure 2.3. Relationship between β and the chain displacement factor in grunerite

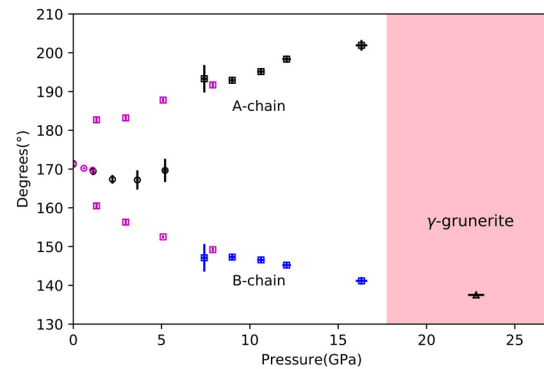


Figure 2.5. O5-O6-O5 kinking angle in grunerite as a function of pressure. The kinking angle of the A chain (black squares) are plotted as 360° minus the O5A-O6A-O5A angle to maintain the same analogy with clinopyroxenes. Circles, squares and triangles are the ambient pressure α -phase, β -phase and high-pressure γ -phase, respectively. Blue squares are the B-chain in the $P2_1/m$ phase. Results from Yang et al. (1998) are shown as magenta markers.

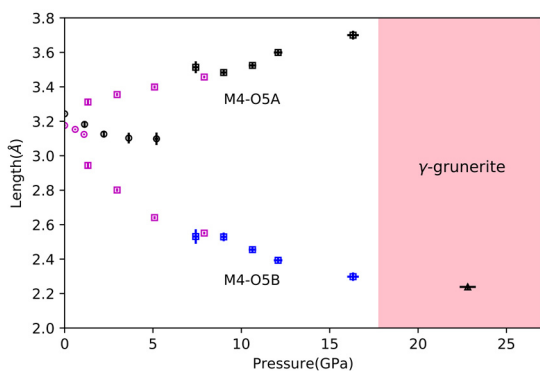


Figure 2.6. Variation of M4-O5 distances in grunerite with pressure. Black squares are M4-O5A distances and blue squares are M4-O5B distances in the β -phase. Results from Yang et al. (1998) are shown as magenta markers.

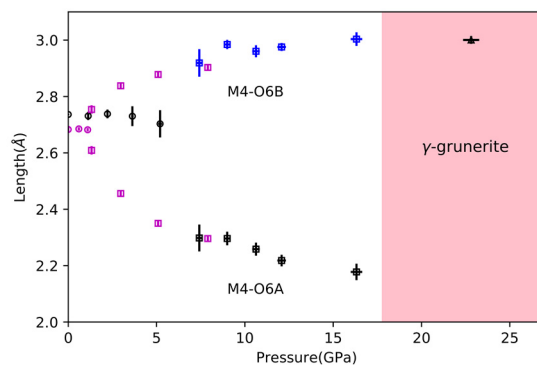


Figure 2.7. Variation of M4-O6 distances in grunerite with pressure. Black squares are M4-O6A distances and blue squares are M4-O6B distances in the β -phase. Results from Yang et al. (1998) are shown as magenta markers.

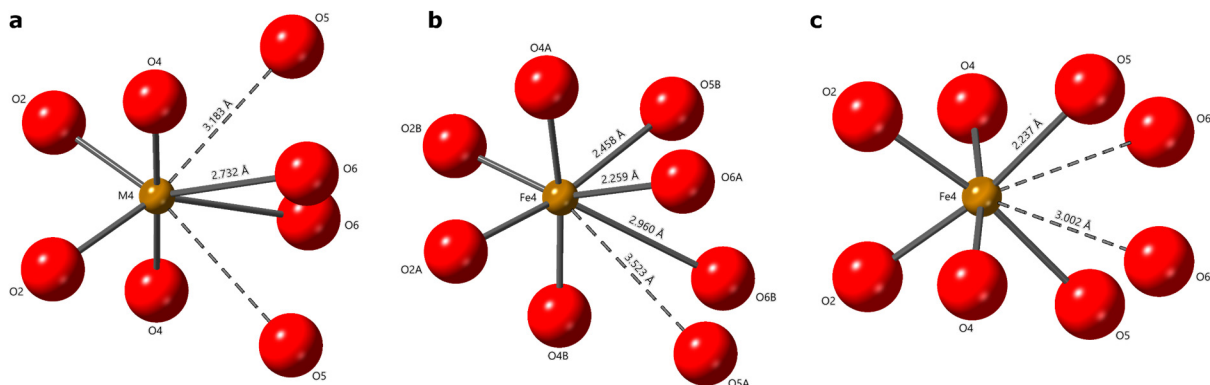


Figure 2.8. Atomic coordination of the M4 cation in grunerite (a) α -grunerite at ambient pressure (b) β -grunerite at 7.4(1) GPa (c) γ -grunerite at 22.8(4) GPa. Dashed lines indicate non-bonding and distances between atoms that are greater than 3 Å.

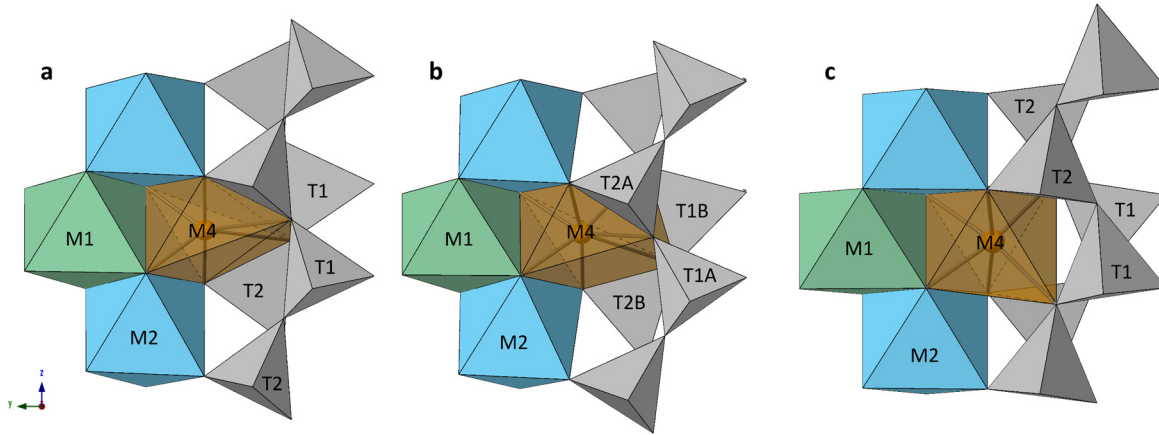


Figure 2.9. M4 polyhedral configuration in grunerite. (a) α -grunerite at ambient pressure, M4 polyhedron sharing edges with M1, 2 x M2 and 2 x T2 polyhedra (b) β -grunerite at 7.4(1) GPa, M4 polyhedron sharing edges with M1, 2 x M2, T1B, T2A and T2B polyhedra (c) γ -grunerite at 22.8(4) GPa, M4 polyhedron sharing edges with M1 and 2 x M2 polyhedra.

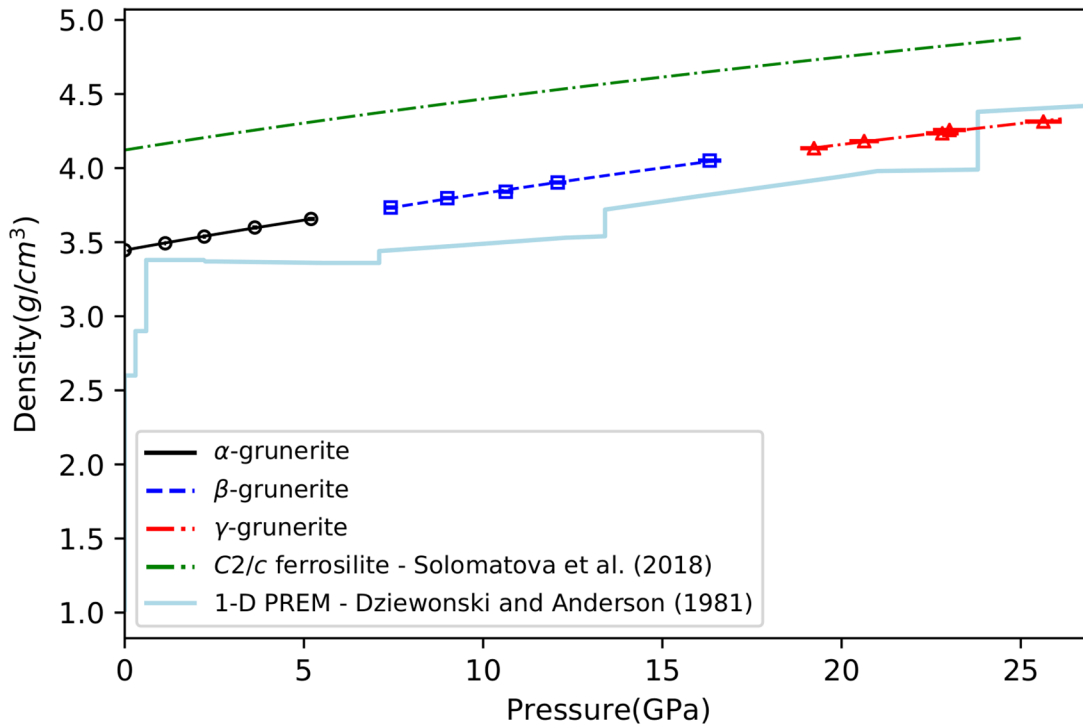


Figure 2.10 Density of the three different polymorphs of grunerite, ferrosilite (Solomatova et al. 2018) and 1-D PREM (Dziewonski and Anderson 1981)

Chapter 3. A New High-Pressure Phase Transition in Natural Gedrite

Abstract

High-pressure diamond-anvil cell synchrotron X-ray diffraction experiments were conducted on single-crystal samples of natural orthoamphibole, gedrite, with composition, $(\text{K}_{0.002}\text{Na}_{0.394})(\text{Mg}_2)(\text{Mg}_{1.637}\text{Fe}_{2.245}\text{Mn}_{0.004}\text{Ca}_{0.022}\text{Cr}_{0.003}\text{Na}_{0.037}\text{Al}_{1.052})(\text{Si}_{6.517}\text{Al}_{1.483})\text{O}_{22}(\text{OH})_2$. The samples were compressed at 298K up to a maximum pressure of 27(1) GPa. In this pressure regime we observed a displacive phase transition between 15.1(7) and 21(1) GPa from the orthorhombic *Pnma* phase to a new structure with space group *P2₁/m*, which is different from the familiar *P2₁/m* structure of cummingtonite and retains the (+, +, -, -) I-beam stacking sequence of the orthorhombic structure. The unit cell parameters for the new phase at 21(1) GPa are $a = 17.514(3)$, $b = 17.077(1)$, $c = 4.9907(2)$ Å and $\beta = 92.882(6)^\circ$. The high-pressure *P2₁/m* phase is the first amphibole structure to show the existence of four crystallographically distinct silicate double chains. The orthorhombic to monoclinic phase transition is characterized by an increase in the degree of kinking on the double silicate chains and is analogous to displacive phase changes recently reported in orthopyroxenes highlighting the parallel structural relations and phase transformation behavior of orthorhombic single- and double-chain silicates. Metastable transformations in amphiboles are important for understanding possible metastability in geologic environments that deviate from an average mantle geotherm, such as cold subducting slabs. These metastable transformations may have possible implications for various petrological and geophysical processes, such as dehydration embrittlement.

This chapter will be published as:

Yong, T., Bina, C., Finkelstein, G., Zhang, D. & Dera, P. A new high-pressure phase transition in natural gedrite.

3.1 Introduction

The amphibole crystal structure is characterized by double chains of silicate tetrahedra that extend along the [001] crystallographic direction. A band of octahedrally coordinated cations, designated by sites M1, M2, M3, and M4, link adjacent chains of silicate tetrahedra, T1A, T1B, T2A and T2B, along the [100] direction. The site symmetries of M1, M2, M3 and M4 are 1, 1, .m. and 1, respectively. In the *Pnma* amphibole structure, there are two distinct types of double silicate chains, the A-chain and B-chain. The structure and crystal chemical relations of amphibole group minerals have been well documented (Papike and Ross 1970; Papike and Cameron 1976; Law and Whittaker 1980; Hawthorne and Oberti 2007).

Gedrite with ideal end-member formula $\text{Mg}_2(\text{Mg}_3\text{Al}_2)(\text{Si}_6\text{Al}_2)\text{O}_{22}(\text{OH})_2$ are among the most crystal-chemically complex amphiboles. Two main coupled substitutions are generally present in gedrites, the first is the substitution of Na^+ in the A-site coupled with the substitution of Al^{3+} for Si^{4+} in the T-sites; the second is the substitution of Al^{3+} for Mg^{2+} in the M-sites coupled with substitution of Al^{3+} for Si^{4+} in the T-sites. The complex nature of gedrites makes them a model structure for understanding high-pressure crystal-chemical relationships and the effects of composition on thermodynamic properties. Knowledge of the non-ambient behavior of gedrites will provide valuable information in modeling various petrological and geophysical processes within the Earth's interior, such as partial melting due to dehydration reactions and water transport to the mantle. At ambient pressure gedrite was found to transform to a new synthetic amphibole 'oxo-gedrite' at 973K indicating dehydrogenation of the gedrite structure (Zema et al. 2012).

The crystallographic, physical and chemical similarities between amphiboles and pyroxenes have been recognized since the 1930s (Warren 1930; Warren and Modell 1930b; Carpenter 1982). Zhang et al. (2012), Dera et al. (2013a) and Finkelstein et al. (2015) showed that

orthopyroxenes undergo a series of phase transformations with increasing pressure from orthorhombic to monoclinic (but preserving orthopyroxene stacking) and back to orthorhombic symmetry. Due to the similarities between amphiboles and pyroxenes, it can be hypothesized that an analogous series of phase transformations exists in orthoamphiboles. Previous high-pressure studies on orthorhombic amphiboles are limited to compressibility measurements (Welch et al. 2011; Nestola et al. 2012) up to 7 GPa and no phase transformations were observed. Until now the high-pressure phase transformation behavior of orthorhombic amphiboles has been unknown. In this study, we report the observations of a new phase transition in natural gedrite, which takes place between 15.1(7) and 21(1) GPa, and leads from *Pnma* (gedrite) to *P2₁/m* (β -gedrite) symmetry.

3.2 Experimental Procedures

Chemical analysis

In this study, we used a natural gedrite crystal from Karelien, Russia, with composition $(K_{0.002}Na_{0.394})(Mg_2)(Mg_{1.637}Fe_{2.245}Mn_{0.004}Ca_{0.022}Cr_{0.003}Na_{0.037}Al_{1.052})(Si_{6.517}Al_{1.483})O_{22}(OH)_2$ determined by wavelength-dispersive spectrometry (WDS) using a JEOL Hyperprobe JXA-8500F. Peaking on standards were done at 15 keV, 20 nA and a beam diameter of 10 μ m. Background corrections were based on measurements either side of the peak during off-peak measurements using a linear correction. Calibration was done at 15 keV, 10 nA and using a beam 10 μ m in diameter. Three spot analyses on two different standards, treated as unknowns, were captured before and after analyses on the samples to look for instrumental errors. Analyses were done with the same analytical conditions as the calibration. The $K\alpha$ lines were used for all elements analyzed. Count times were 30 seconds on peak and 15 seconds on each off-peak position, except for measuring Ca, Cl and K where on peak positions were measured for 20 seconds and off-peak

positions for 10 seconds. Full ZAF corrections to the background-corrected intensities for each spot were made using the Probe for EPMA software (Donovan et al. 2012). The composition was determined through the average of twelve spot analyses. The samples were compositionally homogeneous with no zoning, as evidenced by the electron backscattered image. All iron was assigned as Fe²⁺ to maintain charge balance, however the presence of trace amounts of Fe³⁺ is a possibility. The results from the microprobe analysis are shown in table 3.1 and the measurements of the standards are shown in table 3.2. The chemical formula was calculated based on 23 O atoms as described by Hawthorne and Oberti (2007). This calculation assumes that (O,OH,F,Cl) = 2 apfu and as no F and Cl were detected from the microprobe analysis, we determine there were 2 apfu of OH.

Ambient-pressure X-ray diffraction

To characterize the ambient-pressure crystal structure of the sample used in the high-pressure experiments, a euhedral crystal platelet (0.15 x 0.09 x 0.02 mm) was selected and mounted on a Bruker D8 Venture single crystal diffractometer with a Ag I μ S microfocus source (0.56089 Å) and PHOTON-II CPAD detector at the University of Hawaii at Manoa's X-ray Atlas Diffraction Laboratory. The X-ray diffraction data were collected over a θ range from 2.502 to 30.733° with 98.9% completeness. Least-squares structure refinement was done with the program SHELXL2014 (Sheldrick 2015). The initial structure model of gedrite from Papike and Ross (1970) was used. All atoms were refined using anisotropic atomic displacement parameters except for hydrogen. Hydrogen atom positions were located from the difference Fourier map and then refined using a restraint on the oxygen-hydrogen distance. To the best of our knowledge, hydrogen atom positions in gedrite have not been reported in the literature before. Details on hydrogen-bond

and intermolecular contact interaction geometry in the ambient gedrite phase are reported in table 3.3.

Full occupancy was assumed for all sites except the A site, which was constrained to match the calculated chemical formula from the microprobe analysis. The structure was refined using the chemical formula determined from the microprobe analysis as a restraint, however small amounts of K in the A site (< 0.4 electrons per unit cell) and Mn, Ca, Cr and Na in the M sites (~ 1 electron total contribution per unit cell) were ignored, as X-ray diffraction cannot resolve these small compositional differences. In our refined model the M1, M3, and M4 sites were only occupied by Mg^{2+} and Fe^{2+} , the M2 site was occupied by Al^{3+} , Mg^{2+} and Fe^{2+} , the T1A, T1B and T2B were occupied by both Si^{4+} and Al^{3+} , and the T2A site only contained Si^{4+} . Determination of site occupancies was done following Papike and Ross (1970). Additionally, previous studies of gedrite have shown that there is a strong preference for octahedrally coordinated Al^{3+} in the M2 site (Oberti et al. 2007; Schindler et al. 2008). The determined site occupancies of the four M sites and four T sites are: M1: $\text{Mg}^{2+} = 0.771(4)$, $\text{Fe}^{2+} = 0.228(4)$; M2: $\text{Al}^{3+} = 0.541(4)$, $\text{Mg}^{2+} = 0.401(5)$, $\text{Fe}^{2+} = 0.055(4)$; M3: $\text{Mg}^{2+} = 0.747(6)$, $\text{Fe}^{2+} = 0.252(6)$; M4: $\text{Mg}^{2+} = 0.287(4)$, $\text{Fe}^{2+} = 0.712(4)$; T1A: $\text{Si}^{4+} = 0.74(7)$, $\text{Al}^{3+} = 0.25(7)$; T1B: $\text{Si}^{4+} = 0.60(7)$, $\text{Al}^{3+} = 0.39(7)$; T2A: $\text{Si}^{4+} = 1.0$; T2B: $\text{Si}^{4+} = 0.90(7)$, $\text{Al}^{3+} = 0.09(7)$ Based on these values, our refined chemical formula is $(\text{Na}_{0.393})(\text{Mg}_2)(\text{Mg}_{1.665}\text{Fe}_{2.242}\text{Al}_{1.082})(\text{Si}_{6.48}\text{Al}_{1.46})\text{O}_{22}(\text{OH})_2$, which is in good agreement with our chemical formula obtained by electron microprobe analysis.

High-pressure X-ray diffraction

In-situ high-pressure diffraction experiments were conducted at beamline 13BM-C (GSECARS) of the Advanced Photon Source, Argonne National Laboratory (Zhang et al. 2017). The experiment consisted of six compression measurements at 1.84(9), 4.3(2), 10.6(5), 15.1(7),

21(1) and 27(1) GPa and seven decompression measurements at 24(1), 22(1), 20(1), 15.8(8), 14.2(7), 6.1(3) and 4.0(2) GPa. Two crystals of gedrite with an approximate size of 0.065 x 0.0030 x 0.005 mm were loaded into a 4-pin diamond-anvil cell (DAC) with 300 μm culet diamonds. The crystals were mounted in the DAC in different orientations (approximately [210] and $[\bar{2}\bar{1}0]$ along the DAC axis) to allow for more coverage of reciprocal space. Conical anvils and backing plates (Boehler and De Hantsetters 2004) were used to increase coverage of reciprocal space. The sample chamber consisted of a hole 0.185 mm in diameter that was drilled through a 0.250 mm thick rhenium gasket preindented to a thickness of 0.040 mm. In addition to the sample crystals, two small ruby spheres were placed in the sample chamber as pressure calibrants. The pressure was calculated from the shift of the R1 ruby fluorescence line (Dewaele et al. 2008). The DAC was gas loaded at the GSECARS-COMPRES facility (Rivers et al. 2008) with neon as the pressure medium. After gas loading the cell was at ~ 1.79 GPa and the sample chamber had shrunk to ~ 0.133 mm in diameter. Ruby fluorescence spectra were measured at each pressure point both before and after the X-ray data collection. Reported pressures are from after each X-ray measurement. Uncertainties in pressures were taken as 5% of the pressure measurement.

High-pressure diffraction experiments were performed using a monochromatic X-ray beam with an energy of 28.6 keV (0.434 \AA), and bandwidth of 1 eV, that was focused with a Kirkpatrick-Baez mirror system to a spot of 0.012 mm (H) x 0.018 mm (V), as measured at full width at half maximum (FWHM). The MAR165 charge-coupled device (CCD) detector was placed roughly 180 mm away from the sample, and LaB₆ powder was used to calibrate the distance and tilting of the detector. The sample was placed at the rotation center of the diffractometer and aligned using an optical microscope. A total angular range from $\varphi = 57^\circ$ to 123° (total angular opening of $\pm 33^\circ$) was covered during the scans. A series of step and wide-step φ -exposures were collected. Step

scans involved 1° angular increments, while wide-step scans had 6.6° angular increments. The exposure time was at $5 \text{ sec}/^\circ$. After collection of step and wide-step φ -exposures at the zero detector position, more wide-step φ -exposures were recorded with the detector rotated about its horizontal axis (2θ) by 20° and then with the detector rotated about the vertical axis (ν) by 10° and -10° . Exposure time for the non-zero detector position was at $10 \text{ sec}/^\circ$. At 21(1) GPa, exposure time was increased to $10 \text{ sec}/^\circ$ for the zero detector position and $20 \text{ sec}/^\circ$ for non-zero positions.

Step φ -exposures (13BM-C) were used in reconstruction of the crystal's reciprocal lattice to determine the unit cell parameters and to index the diffraction pattern. Wide-step φ -exposures were used to determine d-spacings, azimuthal angles around the beam center and peak intensities of each diffraction peak in order to solve the crystal structure. Data collection was performed following the procedure described by Dera (2007) and Dera et al. (2013b), and analyzed using the GSE_ADA/RSV program (Dera et al. 2013b). Integrated peak intensities were corrected for Lorenz, polarization, DAC absorption and sample displacement effects using the methods implemented in GSE_ADA. Because of the high incident energy, low absorption coefficient, and negligible sample thickness, the effects of sample absorption were ignored. The linear absorption coefficient at 10.6(5) GPa was 0.751 mm^{-1} and at 21(1) GPa was 0.807 mm^{-1} . Based on these values and our sample thickness of 0.005mm the estimated attenuation of X-ray intensity is less than 1%.

The high-pressure structure at 21(1) GPa was solved by converting the *Pnma* structure model, refined at 10.6(5) GPa before the transition, to the *P2₁/m* setting (*P2₁/m* is a sub-group of *Pnma* and is a direct translationgleiche type I subgroup relation) determined with the use of the program PowderCell 2.4 (Kraus and Nolze 1996). The *P2₁/m* structure could not be refined using the usual *P2₁/m* clinoamphibole structure (cummingtonite structure) despite having the same space

group. The unit cell volume and Z number in the high-pressure gedrite phase are twice the values for cummingtonite. Least-squares structure refinement for selected pressures was done with the program SHELXL2014 (Sheldrick 2015). The procedure for refinement of the high-pressure structure was similar to the ambient pressure phase, however, all atoms in the high-pressure structure were refined with isotropic atomic displacement parameters (ADPs) due to limited coverage of reciprocal space. The site occupancies in all the high-pressure refinements were constrained to those determined from the ambient structure refinement. Polyhedral geometry parameters were calculated using the program VESTA (Momma and Izumi 2011). Details of the crystal structure refinement, refined fractional coordinates for all the atoms, bond lengths and atomic displacement parameters for selected pressures are given in tables 3.4-3.8.

3.3 Results

The transformation of gedrite to β -gedrite takes place between 15.1(7) GPa and 21(1) GPa. This is the first known structural phase transformation reported for an orthorhombic amphibole group mineral. The diffraction pattern at 21(1) GPa was indexed *ab initio* and the unit cell yielded a primitive monoclinic unit cell. The unit cell parameters are $a = 17.514(3) \text{ \AA}$, $b = 17.077(1) \text{ \AA}$, $c = 4.9907(2) \text{ \AA}$, and $\beta = 92.882(5)^\circ$. Here, we report refinements for the orthorhombic gedrite structure up to a maximum pressure of 10.6(5) GPa and the high-pressure monoclinic phase at 21(1) GPa.

At ambient conditions, the unit cell parameters are $a = 18.5383(5) \text{ \AA}$, $b = 17.8286(5) \text{ \AA}$ and $c = 5.2780(1) \text{ \AA}$, which are consistent with Papike and Ross (1970), who reported $a = 18.531(4) \text{ \AA}$, $b = 17.741(4) \text{ \AA}$ and $c = 5.249(5) \text{ \AA}$. At 21(1) GPa we observed a new structure with monoclinic symmetry that we designate as β -gedrite, as evidenced by the appearance of new diffraction peaks, and confirmed by structure solution and refinement

β -gedrite has $P2_1/m$ symmetry, which is the same space group as the low-pressure $P2_1/m$ clinoamphiboles, such as cummingtonite. However, it corresponds to distinctly different structural arrangement, with a double number of formula units per unit cell. Upon decompression to 14.2(7) GPa, the $Pnma$ orthorhombic structure reappeared, as indicated by change in systematic absences. Thus, the transition is entirely reversible. We refined this new structure at 21(1) GPa to an R1 value of 9.6%. The higher R1 value, compared to the orthorhombic structure, is due to a combination of limited coverage in reciprocal space and broadening of diffraction peaks with a larger rocking curve.

In β -gedrite the reduction in symmetry causes a splitting of the Wyckoff positions. The M1, M2 and M4 sites are located on Wyckoff positions 8d in the orthorhombic structure and split into two different sites in the monoclinic structure which occupy Wyckoff positions 4f, where one of the sites is shifted to $(\frac{1}{2} - x, -y, \frac{1}{2} + z)$. Similarly, the A, M3, O3A, O3B, O7A and O7B sites, which occupy Wyckoff position 4c in the orthorhombic structure, split to occupy Wyckoff position 2e, where one site is shifted to $(\frac{1}{2} - x, \frac{1}{4}, \frac{1}{2} - z)$. All remaining oxygen atoms sit on general position 8d and split into two Wyckoff positions 4f in a similar manner to the splitting of the M1, M2, and M4 sites. As a consequence of the Wyckoff positions splitting, there is a doubling in the number of sites in the β -gedrite structure compared to the orthorhombic phase. We define the new sites resulting from the Wyckoff positions splitting with a prime symbol (e.g. M4 site in the gedrite structure splitting to become M4 and M4' in the β -gedrite structure).

A comparison of the crystal structures of gedrite and β -gedrite is shown in figures 3.1 and 3.2. β -gedrite is a novel amphibole structure, showing the existence of four non-equivalent tetrahedral chains. The transformation observed in gedrite from $Pnma$ to $P2_1/m$ symmetry is analogous to the α - β orthopyroxene high-pressure transformation, where the number of

crystallographically distinct silicate chains double from two to four (Zhang et al. 2012; Dera et al. 2013a). We define the new silicate chains that result from the Wyckoff position splitting as A' and B'. Using the bulk modulus and bulk modulus derivative determined from the third-order Birch-Murnaghan equation of state (Nestola et al., 2012), we extrapolate the unit-cell volume of our crystal to be 1507.31 Å³ at 21 GPa in the gedrite phase. The volume discontinuity accompanying the α - β gedrite phase transition is 1.09% compared with a 1.2% volume discontinuity in the α - β opx phase transition (Dera et al., 2013a).

The O5-O6-O5 angle characterizes kinking of the double silicate chains. At ambient conditions, the kinking angle of the A chain and B chain in gedrite are 163.8(1)° and 148.0(1)°, respectively. With pressure increasing to 10.6(5) GPa, the double silicate chains become more kinked (chain shortening), and the angles decrease to 158(1)° and 140.1(9)° for the A chain and B chain. In the new β -gedrite phase at 21(1) GPa, each of the four silicate double chains display extreme kinking with angles of 138.2(9)°, 142.7(8), 134.6(8)° and 134.5(8)° for the A, A', B, B' chain, respectively. During compression in the orthorhombic phase, the sense of rotation for the A and B chain remains O-type (see Papike and Ross (1970) for a review on S- and O-type rotations). As the double silicate chains split into four crystallographically distinct chains, we observe a change in the sense of rotation for the A chain as it becomes S-rotated (figure 3.1). The remaining three chains remain O-rotated in the new monoclinic phase. The change in the sense of rotation for the A chain is comparable to the α - β opx transition (Zhang et al. 2012; Dera et al. 2013a). In the α - β opx transition the SiA and SiB chain, which are both in an O-type configuration in the α -phase, split into four non-equivalent single-chains defined as SiA, SiB, SiC and SiD in the β -phase. The SiB chain converts to an S-type of rotation, while the SiA, SiC, and SiD chains remain O-type, which is analogous to the pressure-induced phase transformation behavior of orthoamphibole

observed in this study. Despite the change in rotation type for the A chain in β -gedrite, the stacking sequence of the I-beams remains the same as in the orthorhombic phase, and can still be described as (+, +, -, -), which is different than the stacking sequence of $P2_1/m$ clinoamphiboles (+, +, +, +). This, again is analogous to the mechanism of the phase transition behavior observed by Zhang et al. (2012) in orthoenstatite where the stacking sequence of the ambient phase is preserved in the high-pressure phase. Figure 3.2 illustrates the I-beam stacking in gedrite, β -gedrite and low-pressure $P2_1/m$ clinoamphiboles.

At ambient pressure, the polyhedral volumes of the M1, M2, M3, and M4 sites are 11.93, 10.47, 11.62, 13.01 \AA^3 , respectively. Quadratic elongation and bond angle variances at ambient pressures are 1.0169 and 53.79 for M1, 1.0068 and 21.97 for M2, 1.0239 and 76.03 for M3, and 1.0666 and 211.47 for M4. At 10.6(5) GPa the polyhedra volumes for the M1, M2, M3, and M4 sites are 11.34, 9.82, 11.10, 11.88 \AA^3 , respectively. Octahedral geometry parameters for M1, M2, M3, and M4 are 1.0114, 1.0052, 1.0150 and 1.0626 for quadratic elongation and 37.90, 17.09, 49.46 and 215.86 for bond angle variance. With increasing pressure, the M1, M2, and M3 polyhedra become more regular, as evidenced by the angle variance and quadratic elongation (Robinson et al. 1971), while the M4 polyhedron becomes slightly more distorted.

In the new β -gedrite phase at 21(1) GPa, polyhedral geometry parameters of the octahedral sites M and M' are in close agreement with each other except for M4 and M4' (table 3.8). The polyhedral volume for M4 and M4' are 12.09 and 10.95 \AA^3 , respectively. M4 and M4' have values of 1.0245 and 1.0381 for quadratic elongation, and 75.68 and 131.61 for bond angle variance. M4 and M4' polyhedra are more regular in the β -gedrite phase, as compared to the ambient gedrite phase, as evidenced by their quadratic elongation and bond angle variance values. By similar reasoning, in the β -gedrite phase, the M4' polyhedron is more distorted than the M4 polyhedron.

The extreme kinking of the double silicate chains, especially in the A-chain, which splits to the A (S-rotated) and A'(O-rotated) chain in β -gedrite (figure 3.1), modifies the coordination environment of the M4 site. In the ambient phase, the M4 central ion is bonded to O2A, O2B, O4A, O4B, O5A, and O5B and the polyhedron shares an edge with the T2A tetrahedra. In the new phase, M4 bonds to O2A, O2B, O4A, O4B, O5B and O6A, and M4' bonds to O2A', O2B', O4A', O4B', O5A', and O5B' (figure 3.3). Due to the shift in the coordination environment of the M4 site, the M4 polyhedron no longer shares any edges with surrounding silicate tetrahedra, while the M4' polyhedron shares one edge with the T2A' tetrahedra (figure 3.4). The absence of edge sharing in the M4 polyhedron leads to an increase in stability due to a decrease in cation-cation repulsion, which is energetically favorable, according to Pauling's rule. The shared edge of the M4' polyhedron causes it to become more distorted than the M4 polyhedron, which is validated by the polyhedral geometry parameters.

3.4 Discussion

Equilibrium phase transformation sequences of the major rock-forming minerals along an average mantle geotherm have been extensively studied. However, metastable behavior under disequilibrium conditions is poorly understood. Metastability may arise from the kinetic hindrance of reactions, due to low temperatures within slabs. The metastable persistence of low-pressure phases into the stability fields of high-pressure phases and spatial variations in mineralogy may contribute to petrological buoyancy forces and have significant geophysical implications such as lateral deflection of slabs at the top of the lower mantle and adiabatic shear instabilities (Bina et al. 2001; Wiens 2001). In olivine and pyroxene, metastability promotes slab stagnation within the transition zone due to low-density metastable phases, which provide positive buoyancy effects (Bina and Kawakatsu 2010; Agrusta et al. 2014; King et al. 2015).

Several studies have been devoted to determining the stability fields of various amphiboles. Akella and Winkler (1966) investigated the stability of gedrite with a series of reactions up to 0.2 GPa and found that the breakdown temperature of gedrite increased with higher pressures. Zema et al. (2012) observed dehydrogenation in gedrite at 973K and ambient pressure with the onset of new behavior in the B-chain at 723K. K-amphibole was found to be stable at pressures up to 16 GPa and below 1200°C (Inoue et al. 1998). Additional experiments on potassic richterite ($\text{KNaCaMg}_5\text{Si}_8\text{O}_{22}(\text{OH})_2$) by Trønnes (2002) have shown that K-richterite is stable to about 1450°C at 9-10 GPa. At higher pressures the Clapeyron slope of amphibole breakdown changes sign, suggesting a lower breakdown temperature at even higher pressures. However, at 1000°C potassic richterite was still stable up to 14 GPa. More recently, Comboni et al. (2018) demonstrated that pargasite, $\text{NaCa}_2(\text{Mg}_4\text{Al})(\text{Si}_6\text{Al}_2)\text{O}_{22}(\text{OH})_2$, is stable up to at least ~ 16.5 GPa and ~ 1200 K without any evidence of de-hydroxylation. In attempting to quantify the effects of the bulk composition of amphiboles, Mandler and Grove (2016) determined that high alkali content stabilizes amphibole to higher pressures and temperatures; high bulk Na/Ca ratios ($\text{Na}_2\text{O}/\text{CaO} > \sim 0.5$) stabilize a highly sodic amphibole to higher pressures at the expense of clinopyroxene; high bulk Na/Ca ratios have lower temperature stability limits, and Ti (and possibly Cr) stabilizes amphibole. It can be asserted from these observations that the stability of amphiboles is highly dependent on their bulk composition. From these previous studies it has been demonstrated that it is possible for the stability fields of certain amphibole species to extend up to ~16 GPa and ~1450°C. Based on the upper limits of these stability fields and the ambient pressure thermal decomposition temperature of gedrite (973K), metastable persistence into higher pressure (~ 20 GPa) but lower temperature domains (< 700°C) is possible.

In estimating the total volume fraction of amphiboles present within a downgoing slab, studies have not considered transport pathways under disequilibrium conditions. It has been estimated that amphiboles can form up to 20-60% of basalts to around 2.4 GPa and roughly 600°C (Yamasaki and Seno 2003) or up to 30-50% by volume in metabasalt between 1 – 3 GPa and over a temperature range of 850 – 1000 °C (Poli and Schmidt 2002). It is possible that a large volume fraction of amphibole remains present within portions of a subducting slab if the slab is very cold, below the amphibole breakdown temperature. Furthermore, in slabs that are colder than expected, due to great age and/or fast subduction velocities, it is conceivable that metastable amphiboles like β -gedrite are preserved to greater depths. Some geophysical and petrological models have assumed that subduction can extend to depths greater than 660 km, while remaining below 700°C (Green and Zhou 1996; Kirby et al. 1996; Bina et al. 2001; Ganguly et al. 2009), suggesting that it is plausible that amphiboles could be metastably transported along disequilibrium pathways to experience pressures higher than 20 GPa while still at temperatures lower than expected for amphibole dissolution or dehydration. As amphiboles react to form denser phases such as clinopyroxenes, orthopyroxenes, olivines, spinels and garnets, metastable preservation of amphiboles would deliver a positive buoyancy effect to the subducting slab. Depending on the volume fraction of metastable amphibole present within the slab, it could potentially contribute to slab stagnation.

The metastable preservation of amphiboles to greater depths has further implications, as they are a source of water for partial melting and devolatilization in subducting slabs. Dehydration reactions in subducting slabs generally liberate water as a fluid phase, which has implications in magmatic and intermediate-depth seismic processes (Bina et al. 2001). Raleigh (1967) observed that dehydration of serpentinite causes weakening as well as changing failure mode from ductile

yielding to shear fracturing. Raleigh and Paterson (1965) suggested that water vapor released from dehydration of hydrous minerals, such as amphiboles, would reduce friction and make brittle fractures possible at greater depths, a process known as dehydration embrittlement. Dehydration embrittlement has been proposed to be an essential mechanism for faulting processes for intermediate and possibly deep earthquakes (Raleigh 1967; Green and Houston 1995; Kirby 1995; Peacock 2001; Hacker et al. 2003; Yamasaki and Seno 2003; Jung et al. 2004; Zahradník et al. 2017). With the metastable preservation of amphibole, dehydration reactions would be expected to occur at higher pressures than previously assumed, and may lead to dehydration embrittlement at greater depths. Jung et al. (2004) suggested that if there are hydrous minerals present and dehydration reactions occur, then dehydration embrittlement could explain all intermediate-depth and possibly even deep earthquakes.

The fairly modest H₂O content of amphiboles, generally 1.5 – 4 wt% (Davidson et al. 2007), would need to be considered, as by contrast serpentine minerals can accommodate up to 13 wt% of H₂O (Wunder et al. 2001; Carlson and Miller 2003). It was previously assumed that dehydration embrittlement enabled shear failure due to production of pore pressure as a consequence of a positive volume change of dehydration reactions and consequent decrease in the effective pressure on existing planes of weakness. Through deformation experiments on antigorite serpentine, Jung et al. (2004) described that the initiation of earthquakes through dehydration embrittlement is not restricted to a positive volume change, but rather involves the separation of fluid from solid reaction products where the density of the fluid is less than the solid phase from which the fluid is derived. Alternatively, Green et al. (2015) hypothesized the existence of an earthquake sliding mechanism that is controlled by phase transformations and demonstrated that nanocrystalline aggregates of solid reaction products promote grain boundary sliding even in the

absence of fluid. Deformation experiments on amphibolite (containing 53% amphibole) have been found similarly to produce several microstructures at the sub-micrometer and nanometer scale (Hacker and Christie 1990). Deformed natural rock samples produced microfaulting as discrete cracks or broad bands of very high dislocation density with local glassy patches and sub-micron scale crystal fragments. Deformed synthetic amphibolite (hot pressed powder of the natural sample) contained several microstructural features probably related to the chemical breakdown of amphibole: 20 nm diameter tubes, pores, and small subhedral neoblasts of pyroxene. Another important observation, using bright-field TEM, is the presence of nanoscale amorphous material in rocks that underwent hydration during eclogite-blueschist transformation in an ancient subduction zone (Konrad-Schmolke et al. 2018). The amorphous material filled a pore between reacting NaCa-amphibole and crystallizing Na-amphibole. These observations from Hacker and Christie (1990) and Konrad-Schmolke et al. (2018) suggest that the dehydration of amphibole is likely to produce nanometric solid products, which may allow for seismogenesis upon dehydration due to the promotion of grain boundary sliding. Furthermore, Ferrand et al. (2017) demonstrated that little dehydration is required to trigger embrittlement through deformation experiments on serpentinized peridotites and proposed that dehydration-driven stress transfer is what causes embrittlement. Consequently, it is likely that dehydration of amphiboles could lead to dehydration embrittlement, even up to 20 GPa, despite the modest H₂O content compared to serpentine minerals. In any case, the complex interplay between metastable preservation, dehydration embrittlement and phase transformation behavior illustrate the potential for metastable amphibole to be a possible trigger for seismic events.

Our study has shown the existence of a new phase of gedrite above 21(1) GPa. This study is the first structural report to show the existence of a phase transition in an orthorhombic

amphibole. The gedrite to β -gedrite phase transition is characterized by the splitting of tetrahedral chains into four crystallographically distinct double silicate chains with smaller kinking angles, the change in rotation type from O-type to S-type in one of the double chains and the shift in M4 site coordination to share one less edge with surrounding polyhedra. Carpenter (1982) concluded that the high-temperature to low-temperature displacive transformations in amphiboles and pyroxenes are exactly analogous, even in the resulting microstructures. The existence of β -gedrite illustrates that this relationship is not limited only to temperature but also extends to pressure, due to the similarities in phase transformation behavior and comparable volume discontinuity in the α - β opx transition. Recent experiments on a clinoamphibole, grunerite, have shown the parallel structural relations and phase transformation behavior of both monoclinic single- and double-chain silicates (Yong et al. 2018), and our study extends this observation to also include orthorhombic inosilicates. As the gedrite to β -gedrite phase transition closely parallels those seen in orthopyroxenes (Zhang et al. 2012; Dera et al. 2013a), it is conceivable that a higher-pressure phase transition back to orthorhombic symmetry exists at higher pressures. Further investigations following disequilibrium pathways that deviate from a mantle adiabat are needed to constrain the thermodynamics and kinetics of metastable transformations, such as the one seen in this study, as they may have significant implications for petrological and geophysical processes.

3.5 Tables and Figures

Table 3.1. Results from microprobe analyses

Constituent	Wt. %	Range	Stand. dev.	Probe standard*	Crystal	Ions/formula
FeO	18.36	17.85 – 18.70	0.29	Garnet, Verma (Mn)	LiF	2.245
MgO	16.69	16.22 – 17.07	0.23	Chromite USNM 117075	TAP	3.637
Na ₂ O	1.52	1.45 – 1.66	0.06	Albite, Amelia	TAP	0.431
Al ₂ O ₃	14.71	14.24 – 15.39	0.37	Chromite USNM 117075	TAP	2.535
SiO ₂	44.57	43.59 – 45.05	0.43	Albite, Amelia	TAP	6.517
CaO	0.14	0.12 – 0.16	0.01	Diopside-2 (UCLA)	PETH	0.022
MnO	0.03	0 – 0.07	0.02	Garnet, Verma (Mn)	LiF	0.004
Cl	0.00	0 – 0.02	0.01	Scapolite	PETH	0
TiO ₂	0.16	0.1 – 0.22	0.03	Sphene glass	LiFH	0
K ₂ O	0.01	0 – 0.03	0.01	Orthoclase (OR-1)	PETH	0.002
Cr ₂ O ₃	0.02	0 – 0.07	0.02	Chromite USNM 117075	LiFH	0.003
Total	96.21					

* Probe standard compositions (Wt.%)

Garnet, Verma (Mn) = SiO₂: 36.88, Al₂O₃: 20.82, FeO: 18.04, CaO: 0.24, MnO: 24.6

Chromite USNM 117075 = Al₂O₃: 9.92, FeO: 13.04, MgO: 15.2, MnO: 0.1, TiO₂: 0.12, Cr₂O₃: 60.5, NiO: 0.16, U₂O₃: 0.09

Albite, Amelia = SiO₂: 68.75, Al₂O₃: 19.43, Fe₂O₃: 0.02, Na₂O: 11.7, K₂O: 0.1

Diopside-2 (UCLA) = SiO₂: 55.27, Al₂O₃: 0.05, FeO: 0.94, MgO: 18.29, CaO: 25.47, MnO: 0.1, Na₂O: 0.05, TiO₂: 0.06

Scapolite = SiO₂: 49.78, Al₂O₃: 25.05, FeO: 0.17, CaO: 13.58, Na₂O: 5.2, K₂O: 0.94, Cl: 1.43, CO₂: 2.5, SO₃: 1.32, H₂O⁺: 0.21

Sphene glass: SiO₂: 30.65, CaO: 28.6, TiO₂: 40.75

Orthoclase (OR-1): SiO₂: 64.39, Al₂O₃: 18.58, FeO: 0.03, Na₂O: 1.14, K₂O: 14.92, BaO: 0.82, SrO: 0.035, NiO: 0.03, U₂O₃: 0.08, SO₃: 0.03, H₂O⁺: 0.08

Table 3.2. Comparison of measured standards as unknowns with published values.

Constituent	Diopside standard			Chromite standard		
	Before	After	Published	Before	After	Published
SiO ₂	55.29(2)	55.27(7)	55.27	0.05(3)	0.05(2)	0
Al ₂ O ₃	0.03(1)	0.04(1)	0.05	9.82(3)	9.92(5)	9.92
FeO	0.93(1)	0.84(9)	0.94	13.23(2)	13.11(1)	13.04
MgO	18.43(1)	18.57(4)	18.29	15.05(4)	15.13(1)	15.2
CaO	25.61(1)	25.35(1)	25.47	0	0	0
MnO	0.08(1)	0.08(3)	0.1	0.20(2)	0.21(3)	0.13
Na ₂ O	0.08(1)	0.07(1)	0.05	0.01(1)	0	0
K ₂ O	0	0	0	0.01(2)	0	0
TiO ₂	0.03(1)	0.05(4)	0.06	0.12(2)	0.10(1)	0.12
Cr ₂ O ₃	0	0	0	61.26(2)	61.61(1)	60.5
Cl	0	0	0	0	0.01(1)	0
Total	100.4	100.27	100.23	99.75	100.14	98.91

Table 3.3. Hydrogen-bond and intermolecular contact interaction geometry

D-H...A	D-H distance (Å)	H...A distance (Å)	D...A distance (Å)	D-H...A angle (°)
O3A – H1...O7A	0.80(2)	3.00(7)	3.475(5)	119(7)
O3B – H2...O7B	0.81(2)	2.43(7)	3.127(4)	143(10)

Table 3.4. Representative single-crystal structure refinement for gedrite at selected pressures

Phase	Gedrite	Gedrite	β-gedrite
Wavelength (Å)	0.560	0.434	0.434
Pressure (GPa)	Ambient	10.6(5)	21(1)
Temperature (K)	298	298	298
θ range for data collection	2.502 – 30.733	2.509 – 23.120	2.472 – 23.133
No. of reflections collected	20450	2898	3083
No. of independent reflections	5597	532	1073
No. of restraints	7	0	0
No. of parameters refined	206	87	173
Limiting indices	-30 ≤ h ≤ 33 -32 ≤ k ≤ 26 -9 ≤ l ≤ 9	-9 ≤ h ≤ 14 -18 ≤ k ≤ 21 -9 ≤ l ≤ 5	-12 ≤ h ≤ 13 -21 ≤ k ≤ 17 -9 ≤ l ≤ 9
Space Group	<i>Pnma</i>	<i>Pnma</i>	<i>P2₁/m</i>
Unit-cell dimensions	a = 18.5385(5) Å b = 17.8286(4) Å c = 5.2780(1) Å	a = 17.823(3) Å b = 17.427(1) Å c = 5.1598(1) Å	a = 17.514(3) Å b = 17.077(1) Å, β = 92.882° c = 4.9907(2) Å
R _{int}	0.0395	0.0976	0.1126
Refinement	F ²	F ²	F ²
Goodness-of-fit on F ²	1.228	1.256	1.184
wR ₂ [I > 2σ(I)]	0.1293	0.1872	0.2026
R ₁ [I > 2σ(I)]	0.0614	0.0846	0.0961

Table 3.5. Refined fractional atomic coordinates and isotropic displacement parameters for gedrite at selected pressures

Atom	x	y	z	Site occupancy	U _{eq}
Gedrite at ambient pressure, <i>Pnma</i> <i>a</i> = 18.5838(5) Å, <i>b</i> = 17.8286(4) Å, <i>c</i> = 5.2780(1) Å					
Na	0.1152(4)	-0.25	0.841(1)	0.393(1)	0.030(1)
Mg1/Fe1	0.12430(4)	0.16089(5)	0.3744(1)	0.771(4)/ 0.228(4)	0.0075(2)
Al2/Mg2/ Fe2	0.12465(5)	0.07248(5)	-0.1259(2)	0.541(4)/0.401(5)/ 0.055(4)	0.0067(2)
Mg3/Fe3	0.12430(6)	0.25	-0.1257(2)	0.747(6)/ 0.252(6)	0.0068(3)
Mg4/Fe4	0.11919(3)	-0.01449(3)	0.3693(1)	0.287(4)/ 0.712(4)	0.0111(1)
Si1A/Al1A	0.23175(4)	-0.16320(5)	-0.4475(1)	0.74(7)/ 0.25(7)	0.0055(3)
Si1B/Al1B	0.01989(4)	-0.16449(5)	0.2960(1)	0.60(7)/ 0.39(7)	0.0065(3)
Si2A	0.22784(4)	-0.07998(5)	-0.2003(1)	1	0.0059(1)
Si2B/Al2B	0.02638(4)	-0.07998(5)	-0.2003(1)	0.90(7)/ 0.09(7)	0.0072(3)
O1A	0.1795(1)	0.1592(1)	0.0369(4)	1	0.0107(3)
O1B	0.0695(1)	0.1584(1)	-0.2854(4)	1	0.0103(3)
O2A	0.1844(1)	0.0745(1)	-0.4398(4)	1	0.0091(3)
O2B	0.0629(1)	0.0745(1)	0.1902(4)	1	0.0111(3)
O3A	0.1806(1)	0.25	-0.4596(6)	1	0.0094(4)
O3B	0.0701(1)	0.25	0.2135(6)	1	0.0092(4)
O4A	0.1862(1)	0.0022(1)	0.0501(4)	1	0.0118(3)
O4B	0.0680(1)	-0.0045(1)	-0.2959(4)	1	0.0115(3)
O5A	0.1970(1)	-0.1113(1)	0.3226(4)	1	0.0132(4)
O5B	0.0541(1)	-0.1025(1)	0.0907(5)	1	0.0160(4)
O6A	0.2026(1)	-0.1315(1)	-0.1747(4)	1	0.0124(3)
O6B	0.0477(1)	-0.1444(1)	-0.4132(5)	1	0.0192(5)
O7A	0.2037(1)	-0.25	0.5219(7)	1	0.0140(5)
O7B	0.0452(1)	-0.25	0.2186(7)	1	0.0125(5)
H1	0.224(1)	0.25	-0.46(1)	1	0.02(2)
H2	0.028(2)	0.25	0.16(2)	1	0.06(3)
Gedrite at 10.6(5) GPa, <i>Pnma</i> <i>a</i> = 17.823 (3) Å, <i>b</i> = 17.427(1) Å, <i>c</i> = 5.1598(1) Å					
Na	0.123(4)	-0.25	0.851(7)	0.393(1)	0.023(9)
Mg1/Fe1	0.1240(6)	0.1631(3)	0.364(1)	0.771(4)/ 0.228(4)	0.006(1)
Al2/Mg2/ Fe2	0.1236(7)	0.0754(4)	-0.135(1)	0.541(4)/0.401(5)/ 0.055(4)	0.009(1)
Mg3/Fe3	0.1234(9)	0.25	-0.134(1)	0.747(6)/ 0.252(6)	0.008(1)
Mg4/Fe4	0.1171(4)	-0.0122(2)	0.3598(7)	0.287(4)/ 0.712(4)	0.0084(8)
Si1A/Al1A	0.2295(8)	-0.1638(4)	-0.451(1)	0.74(7)/	0.007(1)

				0.25(7)	
Si1B/Al1B	0.0263(7)	-0.1655(4)	0.305(1)	0.60(7)/ 0.39(7)	0.005(1)
Si2A	0.2274(8)	-0.0752(4)	0.044(1)	1	0.010(1)
Si2B/Al2B	0.0288(7)	-0.0810(4)	-0.194(1)	0.90(7)/ 0.09(7)	0.009(1)
O1A	0.180(1)	0.1622(9)	0.025(2)	1	0.007(3)
O1B	0.065(1)	0.158(1)	-0.295(3)	1	0.011(4)
O2A	0.183(1)	0.0769(9)	-0.452(3)	1	0.010(3)
O2B	0.061(1)	0.077(1)	0.179(3)	1	0.013(4)
O3A	0.185(2)	0.25	-0.473(4)	1	0.009(5)
O3B	0.064(2)	0.25	0.197(4)	1	0.010(6)
O4A	0.191(1)	0.007(1)	0.038(3)	1	0.011(4)
O4B	0.066(1)	-0.002(1)	-0.299(3)	1	0.018(5)
O5A	0.193(1)	-0.108(1)	0.317(3)	1	0.012(4)
O5B	0.058(1)	-0.0967(9)	0.101(2)	1	0.005(3)
O6A	0.197(1)	-0.137(1)	-0.167(3)	1	0.013(4)
O6B	0.054(1)	-0.150(1)	-0.391(3)	1	0.023(5)
O7A	0.191(2)	-0.25	0.494(4)	1	0.011(6)
O7B	0.055(2)	-0.25	0.203(4)	1	0.006(5)
<hr/>					
β -gedrite at 21(1) GPa, $P2_1/m$					
$a = 17.514(3) \text{ \AA}, b = 17.077(1) \text{ \AA}, c = 4.9907(2) \text{ \AA}, \beta = 82.882(6)^\circ$					
Na	0.381(4)	0.25	0.360(7)	0.393(1)	0.02(1)
Na'	0.870(3)	0.25	0.107(5)	0.393(1)	0.001(5)
Mg1/Fe1	0.1251(6)	0.1635(3)	0.368(1)	0.771(4)/ 0.228(4)	0.004(1)
Mg1'/Fe1'	0.3759(6)	0.8351(3)	0.8272(9)	0.771(4)/ 0.228(4)	0.006(1)
Al2/Mg2/ Fe2	0.1260(7)	0.0755(4)	0.871(1)	0.541(4)/0.401(5)/ 0.055(4)	0.007(1)
Al2'/Mg2'/ Fe2'	0.3757(8)	0.9236(4)	0.327(1)	0.541(4)/0.401(5)/ 0.055(4)	0.011(1)
Mg3/Fe3	0.1249(8)	0.25	0.864(1)	0.747(6)/ 0.252(6)	0.003(1)
Mg3'/Fe3'	0.6214(9)	0.25	0.680(1)	0.747(6)/ 0.252(6)	0.010(1)
Mg4/Fe4	0.1234(4)	0.9844(2)	0.3774(6)	0.287(4)/ 0.712(4)	0.0066(7)
Mg4'/Fe4'	0.3864(4)	0.0077(2)	0.8355(6)	0.287(4)/ 0.712(4)	0.0051(8)
Si1A/Al1A	0.2246(8)	0.8345(4)	0.456(1)	0.74(7)/ 0.25(7)	0.009(1)
Si1A'/Al1A'	0.2752(7)	0.1645(4)	0.052(1)	0.74(7)/ 0.25(7)	0.006(1)
Si1B/Al1B	0.0251(7)	0.8342(4)	0.321(1)	0.60(7)/ 0.39(7)	0.009(1)
Si1B'/Al1B'	0.4703(7)	0.1670(4)	0.815(1)	0.60(7)/ 0.39(7)	0.007(1)
Si2A	0.2253(8)	0.9221(4)	-0.040(1)	1	0.010(1)
Si2A'	0.2762(7)	0.0778(4)	0.544(1)	1	0.008(1)

Si2B/Al2B	0.0283(7)	0.9197(4)	0.821(1)	0.90(7)/ 0.09(7)	0.006(1)
Si2B'/Al2B'	0.4684(8)	0.0817(4)	0.312(1)	0.90(7)/ 0.09(7)	0.008(1)
O1A	0.183(1)	0.1614(9)	0.032(3)	1	0.011(3)
O1A'	0.319(1)	0.8366(1)	0.475(3)	1	0.017(4)
O1B	0.068(1)	0.1599(9)	0.702(2)	1	0.007(3)
O1B'	0.434(1)	0.8391(8)	0.177(2)	1	0.008(3)
O2A	0.184(1)	0.0758(8)	0.562(2)	1	0.005(3)
O2A'	0.315(1)	0.9217(9)	-0.010(2)	1	0.008(3)
O2B	0.060(1)	0.076(1)	0.178(3)	1	0.018(4)
O2B'	0.437(1)	0.917(1)	0.660(3)	1	0.014(4)
O3A	0.192(2)	0.25	0.539(3)	1	0.003(4)
O3A'	0.681(2)	0.25	1.018(3)	1	0.008(4)
O3B	0.062(2)	0.25	0.192(4)	1	0.007(4)
O3B'	0.560(3)	0.25	0.326(4)	1	0.015(5)
O4A	0.192(1)	0.001(1)	0.063(3)	1	0.019(4)
O4A'	0.311(1)	0.996(1)	0.492(3)	1	0.012(4)
O4B	0.064(1)	0.9983(9)	0.702(2)	1	0.006(3)
O4B'	0.438(1)	-0.0002(9)	0.186(2)	1	0.009(3)
O5A	0.196(1)	0.848(1)	0.145(3)	1	0.020(4)
O5A'	0.310(1)	0.0994(9)	0.844(3)	1	0.010(3)
O5B	0.053(1)	0.9053(9)	0.136(2)	1	0.007(3)
O5B'	0.442(1)	0.0944(9)	0.613(3)	1	0.013(4)
O6A	0.194(1)	0.9040(9)	0.650(3)	1	0.009(3)
O6A'	0.303(1)	0.1481(8)	0.364(2)	1	0.005(3)
O6B	0.057(1)	0.844(1)	0.645(3)	1	0.016(4)
O6B'	0.441(1)	0.1556(9)	0.121(3)	1	0.008(3)
O7A	0.806(2)	0.25	0.452(3)	1	0.003(4)
O7A'	0.312(2)	0.25	0.963(4)	1	0.010(5)
O7B	0.944(3)	0.25	0.793(4)	1	0.017(6)
O7B'	0.438(3)	0.25	0.692(4)	1	0.021(6)

Table 3.6. Anisotropic displacement parameters for gedrite at ambient pressure

Atom	U ₁₁	U ₂₂	U ₃₃	U ₂₃	U ₁₃	U ₁₂
Na	0.031(3)	0.023(3)	0.036(3)	0	0.021(3)	0
Mg1/Fe1	0.0080(3)	0.0082(3)	0.0063(3)	0.0009(2)	0.0009(2)	0.0002(2)
Al2/Mg2/Fe2	0.0063(3)	0.0068(3)	0.0070(3)	0.0006(2)	0.0004(2)	0.0001(2)
Mg3/Fe3	0.0076(4)	0.0061(4)	0.0066(4)	0	-0.0000(3)	0
Mg4/Fe4	0.0115(2)	0.0125(2)	0.0094(2)	0.0020(1)	0.0039(1)	0.0034(1)
Si1A/Al1A	0.0045(3)	0.0071(4)	0.0049(3)	-0.0005(2)	-0.004(2)	0.0007(2)
Si1B/Al1B	0.0046(3)	0.0070(4)	0.0078(4)	0.0009(2)	-0.0001(2)	-0.0005(2)
Si2A	0.0045(2)	0.0088(3)	0.0043(2)	-0.0012(2)	-0.0002(2)	0.0009(2)
Si2B/Al2B	0.0047(3)	0.0088(4)	0.0080(4)	0.0025(2)	0.0014(2)	-0.0002(2)
O1A	0.0062(7)	0.0155(9)	0.0104(8)	0.0030(7)	0.0024(6)	0.0023(6)
O1B	0.0075(7)	0.0171(9)	0.0062(7)	0.0018(7)	-0.0010(6)	-0.0025(6)
O2A	0.0051(7)	0.0131(8)	0.0091(7)	0.0012(7)	0.0001(6)	0.0008(6)
O2B	0.0062(7)	0.0111(8)	0.0161(9)	0.0051(7)	-0.0014(7)	0.0003(6)
O3A	0.007(1)	0.011(1)	0.009(1)	0	0.0013(9)	0
O3B	0.008(1)	0.010(1)	0.009(1)	0	-0.0005(9)	0
O4A	0.0090(8)	0.0109(8)	0.0154(9)	-0.0035(7)	-0.0003(7)	0.0026(6)
O4B	0.0112(8)	0.0147(9)	0.0085(8)	0.0035(7)	0.0017(7)	0.0008(7)
O5A	0.0077(8)	0.023(1)	0.0083(8)	0.0041(8)	0.0008(6)	0.0000(7)
O5B	0.0081(8)	0.019(1)	0.020(1)	0.0105(9)	0.0015(7)	0.0014(7)
O6A	0.0082(7)	0.018(1)	0.0104(8)	-0.0085(7)	0.003(6)	-0.0008(7)
O6B	0.0115(9)	0.021(1)	0.025(1)	-0.011(1)	-0.0045(9)	0.0046(8)
O7A	0.011(1)	0.010(1)	0.020(1)	0	0.000(1)	0
O7B	0.011(1)	0.011(1)	0.014(1)	0	-0.000(1)	0

Table 3.7. Unit cell parameters of gedrite at various pressures

Pressure (GPa)	a (Å)	b (Å)	c (Å)	β (°)	V (Å ³)	Space group
0	18.5383(5)	17.8286(4)	5.2780(1)	90	1744.44(1)	<i>Pnma</i>
1.84(9)	18.416(4)	17.754(1)	5.2574(2)	90	1718.9(4)	<i>Pnma</i>
4.3(2)	18.223(5)	17.651(1)	5.2266(3)	90	1681.2(5)	<i>Pnma</i>
10.6(5)	17.823(3)	17.427(1)	5.1598(1)	90	1602.6(3)	<i>Pnma</i>
15.1(7)	17.591(8)	17.301(2)	5.1256(6)	90	1560.0(7)	<i>Pnma</i>
21(1)	17.514(3)	17.077(1)	4.9907(2)	92.882(6)	1490.82(5)	<i>P2₁/m</i>
27(1)	17.247(9)	16.908(3)	4.0907(5)	93.55(1)	1429.06(8)	<i>P2₁/m</i>
24(1)	17.355(4)	16.975(1)	4.9384(2)	93.456(7)	1452.3(3)	<i>P2₁/m</i>
22(1)	17.418(5)	17.016(2)	4.9726(3)	93.214(9)	1471.5(5)	<i>P2₁/m</i>
20(1)	17.456(4)	17.039(1)	4.9915(2)	93.058(8)	1482.5(4)	<i>P2₁/m</i>
15.8(8)	17.605(9)	17.215(3)	5.0390(5)	92.45(1)	1525.8(8)	<i>P2₁/m</i>
14.2(7)	17.585(6)	17.298(2)	5.1245(3)	90	1558.9(5)	<i>Pnma</i>
6.1(3)	18.01(1)	17.570(7)	5.199(1)	90	1646(2)	<i>Pnma</i>
4.0(2)	18.207(5)	17.655(2)	5.2291(3)	90	1680.9(5)	<i>Pnma</i>

Table 3.8. Polyhedra volumes and distortion parameters of gedrite at various pressures

Polyhedra	Average bond length (Å)	Polyhedral Volume (Å ³)	Quadratic elongation	Bond Angle Variance (σ ²)
Gedrite at ambient pressure, <i>Pnma</i>				
M1	2.0934	11.93	1.0169	53.8375
M2	1.9941	10.47	1.0068	21.9492
M3	2.0829	11.62	1.0239	76.1937
M4	2.2025	13.01	1.0666	211.4892
Gedrite at 10.6(5) GPa, <i>Pnma</i>				
M1	2.0527	11.34	1.0114	37.9025
M2	1.9510	9.82	1.0052	17.0948
M3	2.0417	11.10	1.0150	49.4618
M4	2.1360	11.88	1.0626	215.8653
β-gedrite at 21(1) GPa, <i>P2₁/m</i>				
M1	2.0236	10.91	1.0082	26.7785
M1'	1.9844	10.28	1.0086	28.3585
M2	1.9207	9.39	1.0040	13.2891
M2'	1.9211	9.39	1.0048	15.5441
M3	1.9992	10.44	1.0138	46.4812
M3'	1.9764	10.10	1.0124	41.5350
M4	2.1090	12.09	1.0245	75.6850
M4'	2.0552	10.95	1.0381	131.6104

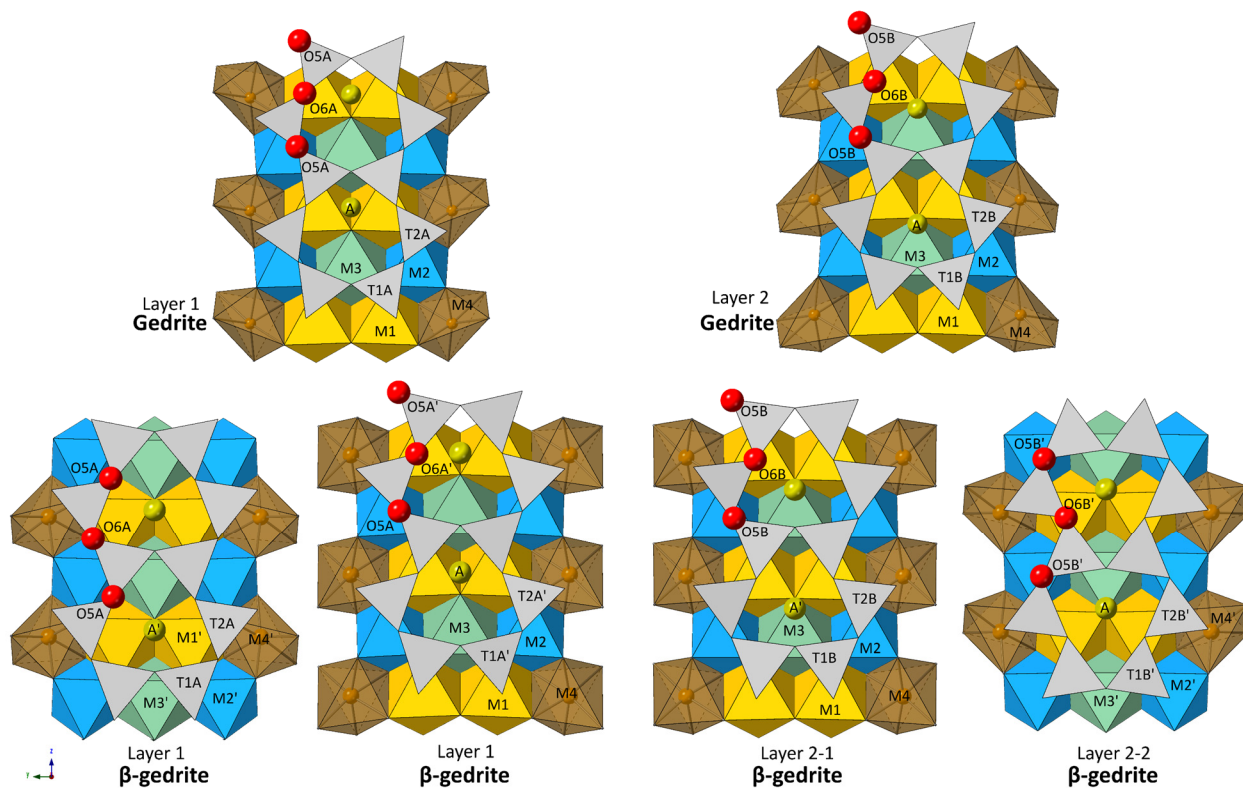
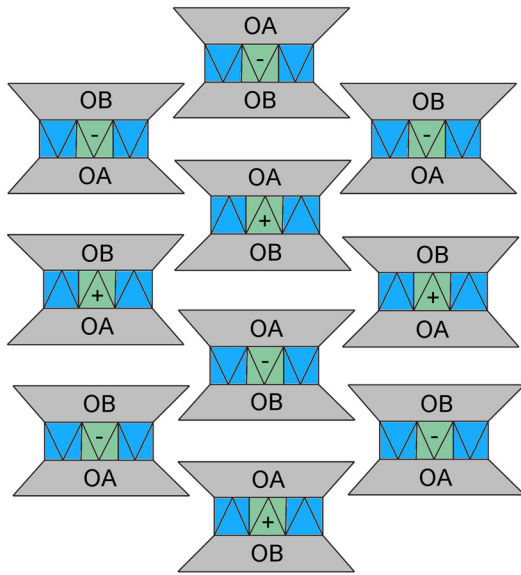
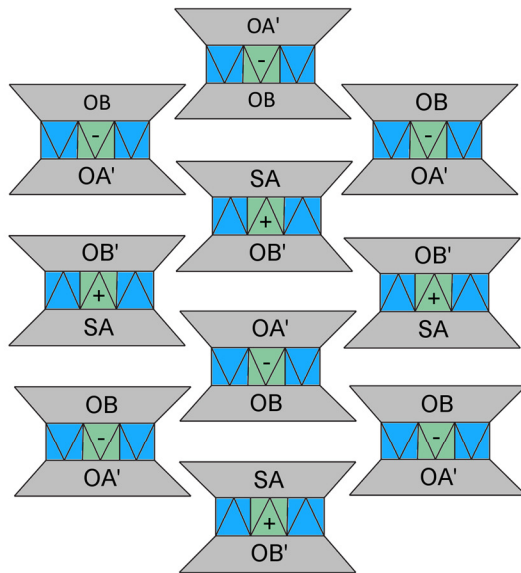


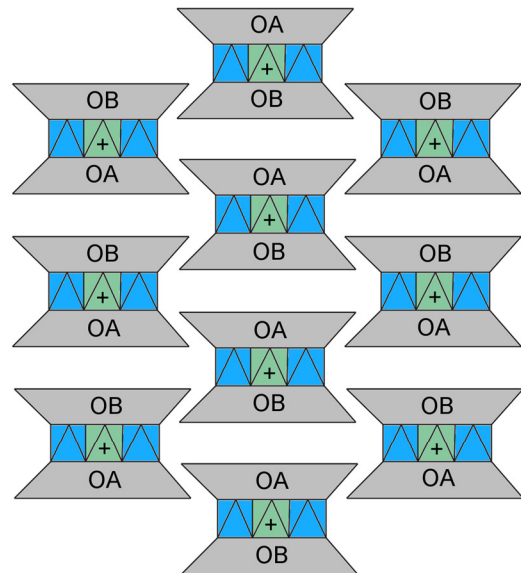
Figure 3.1. (100) projection of the partial structure of gedrite showing the structural changes from gedrite ($Pnma$) to β -gedrite ($P2_1/m$). The reduction in symmetry splits the double-chains of tetrahedra into four nonequivalent chains in the $P2_1/m$ phase. The A chain in the β -gedrite structure has S-type rotation while the A', B and B' chains are O-rotated. Oxygen atoms are shown as red spheres. O5-O6-O5 angles are measured as the obtuse angle.



Gedrite
Pnma



β -gedrite
P2₁/m



Clinoamphibole
P2₁/m

Figure 3.2. I-beam topological representation of gedrite, β -gedrite and $P2_1/m$ clinoamphibole for *ca*. The I-beam stacking sequence in β -gedrite remains the same as the ambient phase (+, +, -, -) despite the change in rotation type for the A-chain. The β -gedrite and $P2_1/m$ clinoamphiboles are different structures as evidenced by their different stacking sequence.

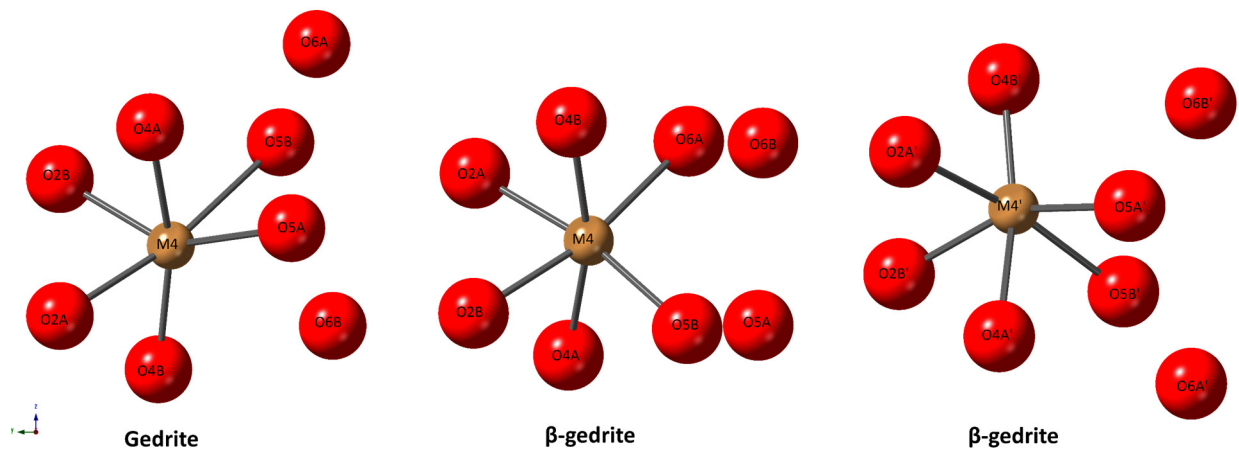


Figure 3.3. Atomic coordination of the M4 cation in gedrite and β -gedrite.

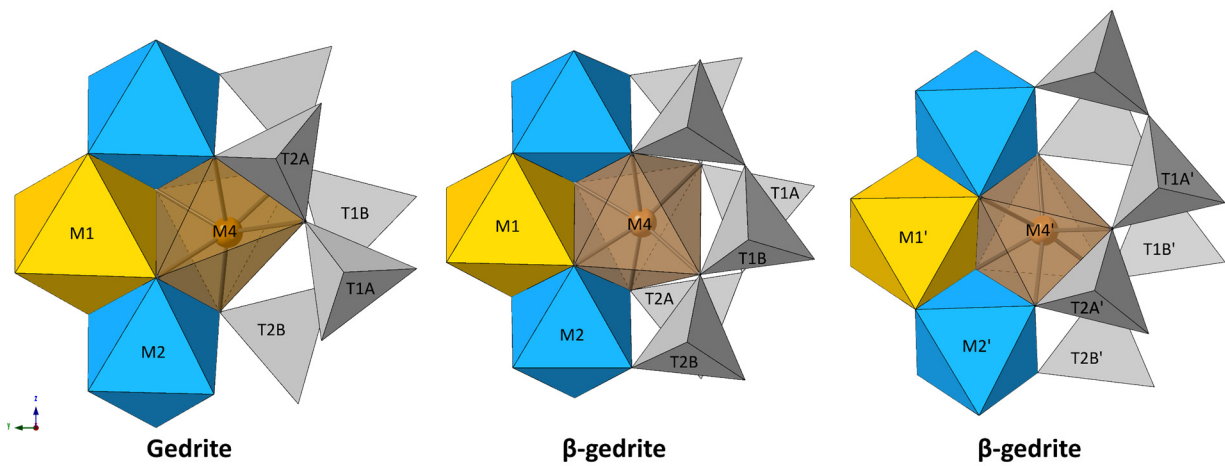


Figure 3.4. M4 polyhedral configuration in gedrite. The M4 polyhedron in β -gedrite is no longer sharing any edges with adjacent tetrahedra from the double-chains.

Chapter 4. Conclusions and Future Work

Two new phases of different amphibole species were discovered at high-pressure through experiments using single-crystal X-ray diffraction. In grunerite (clinoamphibole), the new phase transition adopted a C-centered lattice with space group symmetry $C2/m$ and was isostructural with the ambient phase. In gedrite (orthoamphibole), the new phase transition changed symmetry from orthorhombic ($Pnma$) to monoclinic ($P2_1/m$) and contained four symmetrically independent chains of silicate tetrahedra. The results from this study illustrate the corresponding structural relationships between pyroxenes and amphiboles and demonstrate that the parallel phase transformation behavior is not only limited to temperature as proposed by Carpenter (1982), but also includes pressure. This observation suggests that structures with comparable topology behave similarly in response to high-pressure or high-temperature.

The density of grunerite was determined by single-crystal X-ray diffraction and compared to single-chain pyroxene analog ferrosilite. The density of ferrosilite was shown to be approximately 16% greater than grunerite, supporting the idea that metastable preservation of amphibole could contribute to slab stagnation due to the promotion of positive buoyancy effects. Additionally, the existence of γ -grunerite and β -gedrite illustrate the potential for amphiboles to metastably exist at higher pressures. With the metastable preservation of amphibole, dehydration reactions would likely occur at higher pressures than previously assumed and may lead to dehydration embrittlement at greater depths, especially in geologic environments that are anomalously cold such as cold subducting slabs. This poses the idea that metastable amphibole may be a potential trigger for intermediate or deep earthquakes through the mechanism of dehydration embrittlement.

By nature of their similar structures, pyroxenes and amphiboles may behave similarly in response to high-pressure. This idea could be explored in terms of thermodynamic properties, which have been extensively determined for a wide variety of pyroxenes and their high-pressure phases (Nafziger and Muan 1967; Herzberg 1978; Sharma et al. 1987; Davidson and Lindsley 1989; Angel and Hugh-Jones 1994; Sack and Ghiorso 1994; Powell and Holland 1999). These thermodynamic quantities have not been studied as comprehensively for amphiboles owing to limited P-T range, chemical complexity, and scarcity within the mantle as compared with pyroxenes. Future experiments involving calorimetry or resonant inelastic X-ray scattering could enable determination of these properties. Estimation of these quantities could also be approached theoretically by utilizing density functional theory (DFT) calculations. It would be interesting to see whether any of these properties also behave similarly in response to high-pressure, further illustrating the comparable behavior between the single- and double- chain silicates.

Future experiments involving both high-pressure and high-temperature should be done on both monoclinic and orthorhombic amphiboles up to as high as 1000°C. High-temperature studies up to 1000°C would be ideal as this would cover the temperature range in cold subducting slabs (Ganguly et al. 2009) and may also provide insight on the dehydration temperature of these phases. Neglecting the effects of temperature would be short-sighted as temperature affects the stability field, density and bulk modulus of amphiboles. Therefore, in order to provide accurate determination of these material properties for future geodynamic modelling these high-temperature experiments need to be considered. Simultaneous high-temperature and high-pressure experiments are non-trivial and pose many difficulties, coupled with the chemical and structural complexity of amphiboles these experiments will likely be very challenging.

To further expand on this study, future work should be done on other amphibole compositions to determine if there are any other undiscovered phase transitions and to shed light on the systematics in the high-pressure behavior of amphiboles. This could be done through other experiments utilizing X-ray diffraction at non-ambient conditions or through DFT calculations. The results from this study should be utilized in geodynamic modelling to test the ideas put forth in this thesis.

References

- Agrusta R, Hunen J, Goes S (2014): The effect of metastable pyroxene on the slab dynamics. *Geophysical Research Letters* 41:8800-8808
- Akella J, Winkler HG (1966): Orthorhombic amphibole in some metamorphic reactions. *Contributions to mineralogy and petrology* 12:1-12
- Alvaro M, Nestola F, Ballaran TB, Cámara F, Domeneghetti MC, Tazzoli V (2010): High-pressure phase transition of a natural pigeonite. *American Mineralogist* 95:300-311
- Angel R, Hugh-Jones D (1994): Equations of state and thermodynamic properties of enstatite pyroxenes. *Journal of Geophysical Research: Solid Earth* 99:19777-19783
- Angel RJ (2000): High-Pressure Structural Phase Transitions. *Reviews in Mineralogy and Geochemistry* 39:85-104
- Arlt T, Angel RJ, Miletich R, Armbruster T, Peters T (1998): High-pressure $P2_1/c$ - $C2/c$ phase transitions in clinopyroxenes: Influence of cation size and electronic structure. *American Mineralogist* 83:1176-1181
- Arlt T, Armbruster T (1997): The temperature-dependent $P2_1/c$ - $C2/c$ phase transition in the clinopyroxene kanoite $MnMg[Si_2O_6]$: a single-crystal X-ray and optical study. *European Journal of Mineralogy*:953-964
- Arlt T, Kunz M, Stolz J, Armbruster T, Angel RJ (2000): P-T-X data on $P2_1/c$ -clinopyroxenes and their displacive phase transitions. *Contributions to Mineralogy and Petrology* 138:35-45
- Bina CR, Kawakatsu H (2010): Buoyancy, bending, and seismic visibility in deep slab stagnation. *Physics of the Earth and Planetary Interiors* 183:330-340
- Bina CR, Stein S, Marton FC, Van Ark EM (2001): Implications of slab mineralogy for subduction dynamics. *Physics of the Earth and Planetary Interiors* 127:51-66
- Boehler R, De Hantsetters K (2004): New anvil designs in diamond-cells. *High Pressure Research* 24:391-396
- Boffa Ballaran T, Angel RJ, Carpenter MA (2000): High-pressure transformation behaviour of the cummingtonite-grunerite solid solution. *European Journal of Mineralogy* 12:1195-1213
- Brown G, Prewitt C, Papike J, Sueno S (1972): A comparison of the structures of low and high pigeonite. *Journal of Geophysical Research* 77:5778-5789
- Carlson RL, Miller DJ (2003): Mantle wedge water contents estimated from seismic velocities in partially serpentinized peridotites. *Geophysical Research Letters* 30
- Carpenter M (1982): Amphibole microstructures: some analogies with phase transformations in pyroxenes. *Mineralogical Magazine* 46:395-397
- Comboni D, Lotti P, Gatta GD, Merlini M, Liermann H-P, Frost DJ (2018): Pargasite at high pressure and temperature. *Physics and Chemistry of Minerals* 45:259-278
- Comodi P, Ballaran TB, Zanazzi PF, Capalbo C, Zanetti A, Nazzareni S (2010): The effect of oxo-component on the high-pressure behavior of amphiboles. *American Mineralogist* 95:1042
- Comodi P, Mellini M, Ungaretti L, Zanazzi PF (1991): Compressibility and high pressure structure refinement of tremolite, pargasite and glaucophane. *European Journal of Mineralogy* 3:485-499
- Davidson J, Turner S, Handley H, Macpherson C, Dosseto A (2007): Amphibole “sponge” in arc crust? *Geology* 35:787-790
- Davidson PM, Lindsley DH (1989): Thermodynamic analysis of pyroxene-olivine-quartz equilibria in the system CaO - MgO - FeO - SiO_2 . *American Mineralogist* 74:18-30

- Dera P (2007): GSE-ADA data analysis program for monochromatic single crystal diffraction with area detector. GeoSoilEnviroCARS, Argonne, Illinois
- Dera P, Finkelstein GJ, Duffy TS, Downs RT, Meng Y, Prakapenka V, Tkachev S (2013a): Metastable high-pressure transformations of orthoferrosilite Fs82. *Physics of the Earth and Planetary Interiors* 221:15-21
- Dera P, Zhuravlev K, Prakapenka V, Rivers ML, Finkelstein GJ, Grubor-Urosevic O, Tschauner O, Clark SM, Downs RT (2013b): High pressure single-crystal micro X-ray diffraction analysis with GSE_ADA/RSV software. *High Pressure Research* 33:466-484
- Dewaele A, Torrent M, Loubeyre P, Mezouar M (2008): Compression curves of transition metals in the Mbar range: Experiments and projector augmented-wave calculations. *Physical Review B* 78:104102
- Donovan J, Kremser D, Fournelle J (2012): Probe for EPMA: acquisition, automation and analysis. Probe Software, Inc., Eugene, Oregon
- Downs RT (2003): Topology of the pyroxenes as a function of temperature, pressure, and composition as determined from the procrystal electron density. *American Mineralogist* 88:556-566
- Dziewonski AM, Anderson DL (1981): Preliminary reference Earth model. *Physics of the earth and planetary interiors* 25:297-356
- Ernst WG, Liu J (1998): Experimental phase-equilibrium study of Al- and Ti-contents of calcic amphibole in MORB; a semiquantitative thermobarometer. *American Mineralogist* 83:952-969
- Ferrand TP, Hilairet N, Incel S, Deldicque D, Labrousse L, Gasc J, Renner J, Wang Y, Green Ii HW, Schubnel A (2017): Dehydration-driven stress transfer triggers intermediate-depth earthquakes. *Nature Communications* 8:15247
- Finger LW (1969): The crystal structure and cation distribution of a grunerite. *Mineralogical Society of America Special Paper* 2:95-100
- Finkelstein GJ, Dera PK, Duffy TS (2015): Phase transitions in orthopyroxene (En 90) to 49GPa from single-crystal X-ray diffraction. *Physics of the Earth and Planetary Interiors* 244:78-86
- Fumagalli P, Poli S (2005): Experimentally Determined Phase Relations in Hydrous Peridotites to 6.5 GPa and their Consequences on the Dynamics of Subduction Zones. *Journal of Petrology* 46:555-578
- Ganguly J, Freed AM, Saxena SK (2009): Density profiles of oceanic slabs and surrounding mantle: Integrated thermodynamic and thermal modeling, and implications for the fate of slabs at the 660km discontinuity. *Physics of the Earth and Planetary Interiors* 172:257-267
- Gonzalez-Platas J, Alvaro M, Nestola F, Angel R (2016): EosFit7-GUI: a new graphical user interface for equation of state calculations, analyses and teaching. *Journal of Applied Crystallography* 49:1377-1382
- Green H, Shi F, Bozhilov K, Xia G, Reches (2015): Phase transformation and nanometric flow cause extreme weakening during fault slip. *Nature Geoscience* 8:484
- Green HW, Houston H (1995): The mechanics of deep earthquakes. *Annual Review of Earth and Planetary Sciences* 23:169-213
- Green HW, Zhou Y (1996): Transformation-induced faulting requires an exothermic reaction and explains the cessation of earthquakes at the base of the mantle transition zone. *Tectonophysics* 256:39-56

- Hacker BR, Christie JM (1990): Brittle/ductile and plastic/cataclastic transitions in experimentally deformed and metamorphosed amphibolite. *Geophysical Monograph* 56:127-147
- Hacker BR, Peacock SM, Abers GA, Holloway SD (2003): Subduction factory 2. Are intermediate-depth earthquakes in subducting slabs linked to metamorphic dehydration reactions? *Journal of Geophysical Research: Solid Earth* 108
- Hawthorne FC (1981): Crystal chemistry of the amphiboles. *Reviews in Mineralogy and Geochemistry* 9:1-102
- Hawthorne FC, Oberti R (2007): Amphiboles: Crystal Chemistry. *Reviews in Mineralogy and Geochemistry* 67:1-54
- Herzberg CT (1978): Pyroxene geothermometry and geobarometry: experimental and thermodynamic evaluation of some subsolidus phase relations involving pyroxenes in the system CaO-MgO-Al₂O₃-SiO₂. *Geochimica et Cosmochimica Acta* 42:945-957
- Hirschmann M, Evans BW, Yang H (1994): Composition and temperature dependence of Fe-Mg ordering in cummingtonite-grunerite as determined by X-ray diffraction. *American Mineralogist* 79:862-877
- Hugh-Jones D, Woodland A, Angel R (1994): The structure of high-pressure C2/c ferrosilite and crystal chemistry of high-pressure C2/c pyroxenes. *American Mineralogist* 79:1032-1041
- Iezzi G, Liu Z, Della Ventura G (2006): Synchrotron infrared spectroscopy of synthetic Na(NaMg)Mg₅Si₈O₂₂(OH)² up to 30 GPa: Insight on a new high-pressure amphibole polymorph. *American Mineralogist* 91:479-482
- Iezzi G, Liu Z, Della Ventura G (2009): Synthetic ^ANa^B(Na_xLi_{1-x}Mg₁)^CMg₅Si₈O₂₂(OH)₂ (with x = 0.6, 0.2 and 0) P₂₁/m amphiboles at high pressure: a synchrotron infrared study. *Physics and Chemistry of Minerals* 36:343-354
- Iezzi G, Tribaudino M, Della Ventura G, Margiolaki I (2011): The high-temperature P₂₁/m → C2/m phase transitions in synthetic amphiboles along the richterite-(^BMg)-richterite join. *American Mineralogist* 96:353
- Inoue T, Irifune T, Yurimoto H, Miyagi I (1998): Decomposition of K-amphibole at high pressures and implications for subduction zone volcanism. *Physics of the Earth and Planetary Interiors* 107:221-231
- Jung H, Green Ii HW, Dobrzhinetskaya LF (2004): Intermediate-depth earthquake faulting by dehydration embrittlement with negative volume change. *Nature* 428:545
- King SD, Frost DJ, Rubie DC (2015): Why cold slabs stagnate in the transition zone. *Geology* 43:231-234
- Kirby S (1995): Interslab earthquakes and phase changes in subducting lithosphere. *Reviews of Geophysics* 33:287-297
- Kirby SH, Stein S, Okal EA, Rubie DC (1996): Metastable mantle phase transformations and deep earthquakes in subducting oceanic lithosphere. *Reviews of Geophysics* 34:261-306
- Konrad-Schmolke M, Halama R, Wirth R, Thomen A, Klitscher N, Morales L, Schreiber A, Wilke FD (2018): Mineral dissolution and reprecipitation mediated by an amorphous phase. *Nature communications* 9:1637
- Konzett J, Sweeney RJ, Thompson AB, Ulmer P (1997): Potassium Amphibole Stability in the Upper Mantle: an Experimental Study in a Peralkaline KNCMASH System to 8.5 GPa. *Journal of Petrology* 38:537-568
- Kraus W, Nolze G (1996): POWDER CELL-A Program for the Representation and Manipulation of Crystal Structure and Calculation of the Resulting X-Ray Powder Pattern, pp. 3

- Law AD, Whittaker EJW (1980): Rotated and extended model structures in amphiboles and pyroxenes. *Mineralogical Magazine* 43:565-574
- Mandler BE, Grove TL (2016): Controls on the stability and composition of amphibole in the Earth's mantle. *Contributions to Mineralogy and Petrology* 171:68
- Momma K, Izumi F (2011): VESTA 3 for three-dimensional visualization of crystal, volumetric and morphology data. *Journal of Applied Crystallography* 44:1272-1276
- Nafziger RH, Muan A (1967): Equilibrium phase compositions and thermodynamic properties of olivines and pyroxenes in the system MgO-“FeO” SiO₂. *American Mineralogist: Journal of Earth and Planetary Materials* 52:1364-1385
- Nestola F, Ballaran TB, Ohashi H (2008): The high-pressure C2/c–P2₁/c phase transition along the LiAlSi₂O₆–LiGaSi₂O₆ solid solution. *Physics and Chemistry of Minerals* 35:477-484
- Nestola F, Pasqual F, Welch MD, Oberti R (2012): The effects of composition upon the high-pressure behaviour of amphiboles: compression of gedrite to 7 GPa and a comparison with anthophyllite and proto-amphibole. *Mineralogical Magazine* 76:987
- Niida K, Green DH (1999): Stability and chemical composition of pargasitic amphibole in MORB pyrolite under upper mantle conditions. *Contributions to Mineralogy and Petrology* 135:18-40
- Oberti R, Hawthorne FC, Cannillo E, Cámara F (2007): Long-range order in amphiboles. *Reviews in Mineralogy and Geochemistry* 67:125-171
- Papike J, Ross M (1970): Gedrites-crystal structures and intracrystalline cation distributions. *American Mineralogist* 55:1945-1972
- Papike JJ, Cameron M (1976): Crystal chemistry of silicate minerals of geophysical interest. *Reviews of Geophysics* 14:37-80
- Peacock SM (2001): Are the lower planes of double seismic zones caused by serpentine dehydration in subducting oceanic mantle? *Geology* 29:299-302
- Poli S, Schmidt MW (2002): Petrology of subducted slabs. *Annual Review of Earth and Planetary Sciences* 30:207-235
- Powell R, Holland T (1999): Relating formulations of the thermodynamics of mineral solid solutions; activity modeling of pyroxenes, amphiboles, and micas. *American Mineralogist* 84:1-14
- Prewitt CT, Downs RT (1998): High-pressure crystal chemistry. *Reviews in Mineralogy* 37:283-318
- Prewitt CT, Papike JJ, Ross M (1970): Cumingtonite: A reversible, nonquenchable transition from P2₁/m to C2/m symmetry. *Earth and Planetary Science Letters* 8:448-450
- Raleigh CB (1967): Tectonic Implications of Serpentinite Weakening. *Geophysical Journal International* 14:113-118
- Raleigh CB, Paterson MS (1965): Experimental deformation of serpentinite and its tectonic implications. *Journal of Geophysical Research* 70:3965-3985
- Rivers M, Prakapenka VB, Kubo A, Pullins C, Holl CM, Jacobsen SD (2008): The COMPRES/GSECARS gas-loading system for diamond anvil cells at the Advanced Photon Source. *High Pressure Research* 28:273-292
- Robinson K, Gibbs G, Ribbe P (1971): Quadratic elongation: a quantitative measure of distortion in coordination polyhedra. *Science* 172:567-570
- Sack RO, Ghiorso MS (1994): Thermodynamics of multicomponent pyroxenes: I. Formulation of a general model. *Contributions to Mineralogy and Petrology* 116:277-286

- Schindler M, Sokolova E, Abdu Y, Hawthorne F, Evans B, Ishida K (2008): The crystal chemistry of the gedrite-group amphiboles. I. Crystal structure and site populations. *Mineralogical Magazine* 72:703-730
- Shannon R (1976): Revised effective ionic radii and systematic studies of interatomic distances in halides and chalcogenides. *Acta Crystallographica Section A* 32:751-767
- Sharma K, Agrawal R, Kapoor M (1987): Determination of thermodynamic properties of (Fe, Mg)-pyroxenes at 1000 K by the emf method. *Earth and planetary science letters* 85:302-310
- Sheldrick G (2008): A short history of SHELX. *Acta Crystallographica Section A* 64:112-122
- Sheldrick GM (2015): Crystal structure refinement with SHELXL. *Acta Crystallographica Section C: Structural Chemistry* 71:3-8
- Smyth JR (1974): The high temperature crystal chemistry of clinohypersthene. *American Mineralogist: Journal of Earth and Planetary Materials* 59:1069-1082
- Solomatova NV, Alieva A, Finkelstein GJ, Sturhahn W, Baker MB, Beavers CM, Zhao J, Toellner TS, Jackson JM (2018): High-pressure single-crystal X-ray diffraction and synchrotron Mössbauer study of monoclinic ferrosilite. *Comptes Rendus Geoscience*
- Sueno S, Cameron M, Papike J, Prewitt C (1973): The high temperature crystal chemistry of tremolite. *American Mineralogist* 58:649-664
- Tetzlaff M, Schmelting H (2000): The influence of olivine metastability on deep subduction of oceanic lithosphere. *Physics of the Earth and Planetary Interiors* 120:29-38
- Thompson E, C., Campbell AJ, Liu Z (2016): In-situ infrared spectroscopic studies of hydroxyl in amphiboles at high pressure. *American Mineralogist* 101:706
- Tribaudino M, Nestola F, Meneghini C, Bromiley G (2003): The high-temperature $P2_1/c_1-C2/c$ phase transition in Fe-free Ca-rich $P2_1/c$ clinopyroxenes. *Physics and Chemistry of Minerals* 30:527-535
- Tribaudino M, Prencipe M, Nestola F, Hanfland M (2001): A $P2_1/c-C2/c$ high-pressure phase transition in $Ca_{0.5}Mg_{1.5}Si_2O_6$ clinopyroxene. *American Mineralogist* 86:807-813
- Trønnes R (2002): Stability range and decomposition of potassic richterite and phlogopite end members at 5–15 GPa. *Mineralogy and Petrology* 74:129-148
- Wallace M, Green DH (1991): The effect of bulk rock composition on the stability of amphibole in the upper mantle: Implications for solidus positions and mantle metasomatism. *Mineralogy and Petrology* 44:1-19
- Warren B (1930): II. The structure of tremolite $H_2Ca_2Mg_5(SiO_3)_8$. *Zeitschrift für Kristallographie-Crystalline Materials* 72:42-57
- Warren B, Modell D (1930a): 1. The Structure of Enstatite $MgSiO_3$. *Zeitschrift für Kristallographie-Crystalline Materials* 75:1-14
- Warren B, Modell D (1930b): 11. The Structure of Anthophyllite $H_2Mg_7(SiO_3)_8$. *Zeitschrift für Kristallographie-Crystalline Materials* 75:161-178
- Welch MD, Cámara F, Ventura GD, Iezzi G (2007): Non-Ambient in situ Studies of Amphiboles. *Reviews in Mineralogy and Geochemistry* 67:223-260
- Welch MD, Gatta D, Rotiroti N (2011): The high-pressure behavior of orthorhombic amphiboles. *American Mineralogist* 96:623
- Welch MD, Graham CM (1992): An experimental study of glaucophanic amphiboles in the system $Na_2O-MgO-Al_2O_3-SiO_2-SiF_4$ (NMA SF): some implications for glaucophane stability in natural and synthetic systems at high temperatures and pressures. *Contributions to Mineralogy and Petrology* 111:248-259

- Whittaker E (1960): The crystal chemistry of the amphiboles. *Acta Crystallographica* 13:291-298
- Wiens DA (2001): Seismological constraints on the mechanism of deep earthquakes: Temperature dependence of deep earthquake source properties. *Physics of the Earth and Planetary Interiors* 127:145-163
- Wunder B, Wirth R, Gottschalk M (2001): Antigorite pressure and temperature dependence of polysomatism and water content. *European Journal of Mineralogy* 13:485-496
- Yamasaki T, Seno T (2003): Double seismic zone and dehydration embrittlement of the subducting slab. *Journal of Geophysical Research: Solid Earth* 108
- Yang H, Hazen RM, Prewitt CT, Finger LW, Ren L, Hemley RJ (1998): High-pressure single-crystal X-ray diffraction and infrared spectroscopic studies of the C2/m-P2₁/m phase transition in cummingtonite. *American Mineralogist* 83:288-299
- Yang H, Prewitt CT (2000): Chain and Layer Silicates at High Temperatures and Pressures. *Reviews in Mineralogy and Geochemistry* 41:211-255
- Yong T, Dera P, Zhang D (2018): Single-crystal X-ray diffraction of grunerite up to 25.6 GPa: a new high-pressure clinoamphibole polymorph. *Physics and Chemistry of Minerals*
- Zahradník J, Čížková H, Bina CR, Sokos E, Janský J, Tavera H, Carvalho J (2017): A recent deep earthquake doublet in light of long-term evolution of Nazca subduction. *Scientific Reports* 7:45153
- Zanazzi PF, Nestola F, Pasqual D (2010): Compressibility of protoamphibole: A high-pressure single-crystal diffraction study of protomangano-ferro-anthophyllite. *American Mineralogist* 95:1758
- Zema M, Welch MD, Oberti R (2012): High-T behaviour of gedrite: thermoelasticity, cation ordering and dehydrogenation. *Contributions to Mineralogy and Petrology* 163:923-937
- Zhang D, Dera PK, Eng PJ, Stubbs JE, Zhang JS, Prakapenka VB, Rivers ML (2017): High pressure single crystal diffraction at PX². *Journal of visualized experiments: JoVE*
- Zhang JS, Dera P, Bass JD (2012): A new high-pressure phase transition in natural Fe-bearing orthoenstatite. *American Mineralogist* 97:1070-1074
- Zhang L, Ahsbahs H, Kutoglu A, Hafner SS (1992): Compressibility of grunerite. *American Mineralogist* 77:480-483